

# GA-NIFS: A smouldering disk galaxy undergoing ordered rotation at $z = 4.26$

Gareth C. Jones<sup>1,2★</sup>, Roberto Maiolino<sup>1,2,3</sup>, Francesco D'Eugenio<sup>1,2</sup>, Santiago Arribas<sup>4</sup>, Andrew J. Bunker<sup>5</sup>, Stephane Charlot<sup>6</sup>, Michele Perna<sup>4</sup>, Bruno Rodriguez del Pino<sup>4</sup>, Hannah Übler<sup>7</sup>, Torsten Böker<sup>8</sup>, Giovanni Cresci<sup>9</sup>, Isabella Lamperti<sup>10,9</sup>, Eleonora Parlanti<sup>11</sup>, Robert Pascalau<sup>1,2</sup>, Jan Scholtz<sup>1,2</sup>, Sandra Zamora<sup>11</sup>

<sup>1</sup>Kavli Institute for Cosmology, University of Cambridge, Madingley Road, Cambridge CB3 0HA, UK

<sup>2</sup>Cavendish Laboratory, University of Cambridge, 19 JJ Thomson Avenue, Cambridge CB3 0HE, UK

<sup>3</sup>Department of Physics and Astronomy, University College London, Gower Street, London WC1E 6BT, UK

<sup>4</sup>Centro de Astrobiología (CAB), CSIC-INTA, Ctra. de Ajalvir km 4, Torrejón de Ardoz, E-28850, Madrid, Spain

<sup>5</sup>Department of Physics, University of Oxford, Denys Wilkinson Building, Keble Road, Oxford OX1 3RH, UK

<sup>6</sup>Sorbonne Université, CNRS, UMR 7095, Institut d'Astrophysique de Paris, 98 bis bd Arago, 75014 Paris, France

<sup>7</sup>Max-Planck-Institut für extraterrestrische Physik, Gießenbachstraße 1, 85748 Garching, Germany

<sup>8</sup>European Space Agency, c/o Space Telescope Science Institute, 3700 San Martin Drive, Baltimore MD 21218, USA

<sup>9</sup>INAF - Osservatorio Astrofisico di Arcetri, largo E. Fermi 5, 50127 Firenze, Italy

<sup>10</sup>Dipartimento di Fisica e Astronomia, Università di Firenze, Via G. Sansone 1, 50019, Sesto F.no (Firenze), Italy

<sup>11</sup>Scuola Normale Superiore, Piazza dei Cavalieri 7, I-56126 Pisa, Italy

Accepted XXX. Received YYY; in original form ZZZ

## ABSTRACT

Rotating galaxies with relaxed gaseous disks have been discovered across cosmic time, from the local Universe to high redshift ( $z > 4$ ). But few such sources have been confirmed at  $z > 4$ , making them a precious sample to examine what conditions result in such ordered kinematics in an early, more chaotic Universe. One of the best examples of this sample is the galaxy DLA0817g1 ( $z = 4.2603$ ), which shows remarkably clear rotation in ALMA [C II] data. We present recent JWST/NIRSpec IFU data ( $R \sim 2700$ ) of DLA0817g1, which we combine with archival ALMA [C II] observations to place constraints on its ISM conditions and morpho-kinematics. From a combination of line ratios, we find a high gas-phase metallicity ( $\sim 0.7 Z_{\odot}$ ), high fraction of obscured star formation, low ionisation (compared to other high-redshift galaxies observed with JWST), and no significant evidence for AGN (based on the WHAN diagnostic). Dynamical modelling with <sup>3D</sup>Barolo reveal nearly identical rotation in H $\alpha$  and [C II], but with a higher velocity dispersion in the former. Using our metallicity estimate and previous CO and [C II] detections, we derive a new estimate of the molecular gas mass, relieving a previous strain in the mass budget. Altogether, we suggest that this is a ‘smouldering’ galaxy, where past star formation resulted in significant chemical enrichment (i.e.,  $Z_{\text{gas}}$  and  $M_{\text{dust}}$ ), but the current activity is low (i.e., lower ionisation parameter and electron temperature). These new observations have opened a window into questions regarding the interplay of gas, metallicity, star formation, and kinematics in a prototypical early disk galaxy.

**Key words:** galaxies: high-redshift – galaxies: kinematics and dynamics – galaxies: disc – galaxies: evolution – galaxies: ISM

## 1 INTRODUCTION

The study of rotating galaxies is a historic field, with observations dating back more than a century. Following the detection of rotation in the Andromeda Galaxy (e.g., Slipher 1914; Pease 1918), it was soon found that our Galaxy is also rotating (e.g., Lindblad 1927; Oort 1927). Similar observations of nearby galaxies showed that they feature rotation as well (e.g., Mayall & Aller 1942; Burbidge & Burbidge 1959; Burbidge et al. 1960; de Vaucouleurs 1961; de Vaucouleurs

& de Vaucouleurs 1962; Takase 1967; Casertano 1983). Each study resulted in a ‘rotation curve’, or a radial profile of rotational velocity (usually taken along the kinematic major axis).

A major step forward came with the work of Rubin et al. (1980), who found that the rotation curves of their observed galaxies did not rise and fall with radius, as expected from the observed baryonic matter distribution. Instead, the curves rose quickly and then were either flat or rose slowly, implying the presence of an additional, unobserved mass component (i.e., non-baryonic or dark matter). By observing the baryonic mass distribution of galaxies (i.e., gas, dust, stars), calculating the total dynamical mass from the observed kine-

★ E-mail: gj283@cam.ac.uk

matics, and subtracting the two, the dark matter component of a galaxy may be found (e.g., [van Albada et al. 1985](#); [Begeman et al. 1991](#); [Sofue & Rubin 2001](#); [Förster Schreiber et al. 2009](#); [Wuyts et al. 2016](#); [Fraternali et al. 2021](#)).

Large samples of galaxy rotation curves for sources beyond the local Universe have now been measured using the  $H\alpha$  line, including the programs ‘Assessing the Mass-Abundance redshift Evolution’ (AMAZE;  $3.0 < z < 5.2$ ; [Maiolino et al. 2008](#)), ‘Lyman-break galaxies Stellar populations and Dynamics’ (LSD;  $2.4 < z < 3.4$ ; [Mannucci et al. 2009](#)), ‘Spectroscopic Imaging survey in the Near-infrared with SINFONI’ (SINS;  $1 \lesssim z \lesssim 3$ ; [Förster Schreiber et al. 2009](#)), ‘The KMOS Redshift One Spectroscopic Survey’ (KROSS;  $z \sim 1$ ; [Stott et al. 2016](#); [Tiley et al. 2016](#)), and KMOS<sup>3D</sup> ( $0.6 \lesssim z \lesssim 2.7$ ; [Wisnioski et al. 2019](#)).

Historically, the kinematics of galaxies at higher redshift ( $z \gtrsim 3$ ) have been studied using far-infrared lines (e.g., CO, [C II]  $158\mu\text{m}$ ; hereafter [C II]) rather than rest-optical lines due to instrumental restrictions and atmospheric effects. Large surveys of [C II] emission include ‘Tracing Rotation with Ionized Carbon in Early Primeval Systems’ (TRICEPS;  $4 < z < 5$ ; [Lelli et al. in prep](#)), ‘The Atacama Large Millimeter Array (ALMA) Large Program to INvestigate [C II] at Early times’ (ALPINE;  $4 < z < 6$ ; [Le Fèvre et al. 2020](#)) with the follow-up program ‘[C II] Resolved ISM in Star-forming Galaxies with ALMA’ (CRISTAL; [Herrera-Camus et al. 2025](#)), and the ‘Reionization Era Bright Emission Line Survey’ (REBELS;  $6.6 < z < 8.6$ ; [Bouwens et al. 2022](#)).

While rest-frame optical and far-infrared (FIR) lines are both strong indicators of the underlying kinematics of a galaxy (i.e., rotation, merging, in-/outflows), their different emission conditions mean that they trace different phases of the interstellar medium (ISM). For example, since the ionisation potential of ionised carbon (11.3 eV; e.g., [Accurso et al. 2017](#)) is lower than that of neutral hydrogen (13.6 eV), [C II] may emanate from the cold or warm neutral medium, warm and dense molecular gas, or warm ionised medium (e.g., [Wolfire et al. 2003](#); [Pineda et al. 2013](#)). On the other hand, doubly ionised oxygen has a higher ionisation potential (35.1 eV; e.g., [Ramos Padilla et al. 2023](#)), meaning that [O III] $\lambda 5007$  traces hot ionised gas. This can also be seen in temperature-density plots of cosmological simulations (e.g., [Schimek et al. 2024](#); [Choustikov et al. 2025](#)), where [O III] $\lambda 5007$  and [O III] $88\mu\text{m}$  only come from warmer gas, while [C II] emanates from warm and cold gas, and CO originates from colder gas.

Due to their different excitation mechanisms, observations have found that ionised gas features a higher velocity dispersion than colder gas (e.g., [Cortese et al. 2017](#); [Übler et al. 2019](#); [Girard et al. 2021](#); [Rizzo et al. 2024](#); [Fujimoto et al. 2025](#)). [Parlanti et al. \(2024\)](#) found a higher ionised velocity dispersion in the centre of ALESS73.1, but ascribe this to feedback from an active galactic nucleus (AGN). On the other hand, some galaxies have found molecular and ionised velocity dispersions that are comparable (e.g., [Genzel et al. 2013](#); [Übler et al. 2018](#); [Molina et al. 2019b](#); [Arribas et al. 2024](#)). While rotation curves of both tracers are similar, some galaxies show higher rotation velocities in the colder phase (e.g., [Davis et al. 2013](#); [Levy et al. 2018](#)). Simulations have shown that molecular tracers (e.g., [C II]) likely probe the gaseous disk of galaxies while ionised tracers (e.g.,  $H\alpha$ ) include contributions from extra-planar ionised gas that increase the observed dispersion (e.g., [Kohandel et al. 2024](#)). Additional observations of both the ionised and molecular gas kinematics of rotating disk galaxies are required to determine how the rotational velocity and velocity dispersion of each evolve with cosmic time - informing models of feedback from AGN and star formation, mass evolution, and galaxy formation.

Observations with the Integral Field Unit (IFU) of the JWST/NIRSpec instrument ([Böker et al. 2022](#); [Jakobsen et al. 2022](#)) have enabled detailed characterisation of galaxy morpho-kinematics and ISM conditions from the local Universe (e.g., [Lai et al. 2023](#); [Bianchin et al. 2024](#); [Perna et al. 2024](#); [Ceci et al. 2025](#); [Taylor et al. 2025](#); [Ulivi et al. 2025](#)) to the first  $\sim 500$  Myr of cosmic time (e.g., [Maiolino et al. 2024](#); [Scholtz et al. 2024](#); [Marconcini et al. 2024](#); [Xu et al. 2024](#)). The high spatial resolution of this instrument opens a clear window into the kinematics of each source. In fact, NIRSpec IFU observations of rest-optical emission lines from some galaxies that were classified as rotators based on ALMA [C II] observations revealed the presence of multiple smaller galaxies (e.g., HZ10, [Jones et al. 2017, 2025b](#); COS-3018, [Smit et al. 2018](#); [Scholtz et al. 2025a](#); HZ4, [Jones et al. 2021](#); [Parlanti et al. 2025](#)). Other previously classified rotators were confirmed, but with a combination of strong inflows, outflows, and/or an AGN component (e.g., ALESS73.1, [Lelli et al. 2021](#); [Parlanti et al. 2024](#); BR1202-0725-SMG, [Carniani et al. 2013](#); [Zamora et al. 2025](#); GN20, [Hodge et al. 2012](#); [Übler et al. 2024](#)). In this context, we will discuss JWST/NIRSpec IFU observations of the galaxy ALMA J081740.85+135138.2 ( $z = 4.2603$ ; hereafter DLA0817g1), a well-studied [C II] rotator.

DLA0817g1 was detected as the host galaxy of a high metallicity damped Lyman-alpha absorber (DLA) at an angular separation of  $\sim 6''$  from a background quasar (QSO J081740.52+135134.5;  $z = 4.398$ ; [Rafelski et al. 2012](#)). ALMA observations at  $\sim 0.8''$  resolution ( $\sim 6.1$  kpc) of the [C II] and rest-frame FIR emission showed a strong detection with an evident velocity gradient ([Jones et al. 2017](#); [Neeleman et al. 2017](#)). Follow-up ALMA [C II] observations at higher resolution ( $\sim 0.19''$ ;  $\sim 1.3$  kpc) confirmed that the galaxy kinematics are well-modelled by a rotation-dominated disk with a dynamical mass of  $\log_{10}(M_{\text{dyn}}/M_{\odot}) = 10.9^{+0.2}_{-0.3}$  within the central  $r \sim 4$  kpc (as derived using different dynamical models; e.g., [Neeleman et al. 2020](#); [Jones et al. 2021](#)).

[Neeleman et al. \(2020\)](#) found that DLA0817g1 features a very low star formation rate (SFR) based on rest-frame near-UV observations (HST/WFC3 F160W;  $SFR_{\text{NUV}} = 16 \pm 3 M_{\odot} \text{ yr}^{-1}$ ), but a considerable [C II]-based SFR ( $SFR_{[\text{CII}]} = 420 \pm 260 M_{\odot} \text{ yr}^{-1}$ ) and rest-frame FIR-based SFR ( $SFR_{160\mu\text{m}} = 118 \pm 14 M_{\odot} \text{ yr}^{-1}$ ). Using a detection of CO(2-1) with the The Karl G. Jansky Very Large Array (JVLA), they estimate the molecular gas mass to be comparable to the previously determined dynamical mass:  $\log_{10}(M_{\text{H}_2}/M_{\odot}) = 10.9^{+0.1}_{-0.2}$  (assuming  $r_{21} = 0.81$ ,  $\alpha_{\text{CO}} = 3.0 M_{\odot} \text{ K}^{-1} \text{ km}^{-1} \text{ s pc}^{-2}$ ). Since this CO(2-1) detection is spatially unresolved, it represents the gas mass within a radius of  $\sim 7$  kpc.

Altogether, this suggests that DLA0817g1 is a gas-rich, rotating, star-forming galaxy in the early Universe ( $t_{\text{H}} \sim 1.4$  Gyr). But there are several mysteries that still surround this source. Primarily, the dynamical and gas masses are comparable to within  $1\sigma$ , which leaves little room for stellar mass or a dark matter component ( $M_{\text{dyn}} = M_{\star} + M_{\text{H}_2} + M_{\text{dust}} + M_{\text{DM}} + \dots$ ). This suggests that the conversion factors used to estimate  $M_{\text{H}_2}$  can be incorrect, and that metallicity measurements are required to correctly calibrate the gas mass measurements (e.g., [Madden et al. 2020](#); [Vallini et al. 2025](#)). In addition, [Neeleman et al. \(2017\)](#) argue that the kinematic properties of the galaxy derived through [C II] observations (i.e.,  $v_{\text{rot}}/\sigma_v \sim 3.4$ , Toomre  $Q \sim 1$ ) suggest a relaxed, rotating disk formed through filamentary accretion. But since most of the analysis of this source has been performed on rest-FIR data, the ISM properties are not well constrained (e.g., temperature, metallicity, ionization).

In this work, we present new JWST/NIRSpec IFU observations of DLA0817g1, opening a window into the ionised gas kinematics, ISM conditions, and general nature of this galaxy. In Section 2, we provide

details of our NIRSpec IFU observations and calibration, as well as those of archival ALMA data that we use for comparison. This is followed by a resolved and integrated spectral analysis (Section 3), and an application of <sup>3D</sup>Barolo to our data (Section 4). We discuss our findings in Section 5 and conclude in Section 6. Throughout, we assume a concordance cosmology ( $h_0 = 0.7$ ,  $\Omega_m = 0.3$ ,  $\Omega_\Lambda = 0.7$ ), where 1 kpc = 6.8 kpc at the redshift of our source ( $z = 4.26$ ).

## 2 OBSERVATIONS AND CALIBRATION

### 2.1 JWST

The JWST/NIRSpec IFU data studied in this work originate from the ‘Galaxy Assembly with NIRSpec Integral Field Spectroscopy’ (GA-NIFS<sup>1</sup>) Guaranteed Time Observations (GTO) program (PIs: R. Maiolino & S. Arribas). DLA0817g1 (08h17m40.8680s +13°51′38.22″) was observed as part of PID 4528 (PI: K. Isaak) for 3.53 hours on 8 December, 2024 with the disperser/filter combination G395H/F290LP (hereafter R2700,  $2.87 \mu\text{m} < \lambda_{\text{obs}} < 5.14 \mu\text{m}$ ,  $5450 \text{ \AA} \leq \lambda_{\text{rest}} \leq 9770 \text{ \AA}$ ) using a 6-point medium cycling dither pattern, the NRSIRS2RAPID readout pattern (Rauscher et al. 2017), and 88 groups per integration. We note that the quasar associated with DLA0817g1 (QSO J081740.52+135134) is  $\sim 6''$  from our target (e.g., Neeleman et al. 2017) and is therefore not covered by our observations.

The raw data from these observations were downloaded from the MAST archive<sup>2</sup>. Calibration was performed using a customised version of the STScI pipeline (v1.15.1; Bushouse et al. 2024; see Perna et al. 2023 for more details of customisation) with CRDS context 1303. These customisations account for 1/f noise correction, drizzling (Fruchter & Hook 2002), the subtraction of median values from count rate maps, manually masked cosmic rays and snowballs, open MSA slits, and outlier rejection (95%, D’Eugenio et al. 2024). This results in a calibrated data cube with spaxels of  $0.05''$ .

Next, we performed background subtraction using the observed data cube. Using a conservative mask based on the H $\alpha$  emission, we mask DLA0817g1, and for each spectral channel of the original data cube we find the mean value of the unmasked values that lie on the same slicers (in the spatial or cross-dispersion direction) as DLA0817g1. These are used to generate a background cube, which is subtracted from the cube. We then mask all spaxels at different slicers, as they lack a background correction.

Since we wish to compare the JWST/NIRSpec data to ALMA images, it is important to verify the astrometry of our data. By comparing our NIRSpec data to archival NIRCам data (aligned to the Gaia DR3 reference frame), we find a spatial offset of  $\sim 0.1''$ , which is expected from the JWST pointing uncertainty with no target acquisition (see full details in Appendix A). We correct for this offset, resulting in a positional uncertainty of  $\sim 0.01''$ .

It is important to account for the wavelength-dependent PSF of our data, as we will compare emission across the full wavelength range of our data (e.g., [S III] $\lambda$ 9532 and [S II] $\lambda$ 6731). To do this, we create a PSF-matched cube by convolving each spectral channel of our data cube with a custom kernel (see Appendix B for details). The resulting cube has a uniform PSF that can be approximated by a Gaussian with FWHM  $0.22''$ .

Previous works (e.g., Übler et al. 2024) have shown that the ‘ERR’

extension of pipeline-calibrated IFU data is useful for characterising the wavelength-dependent noise behaviour of the data, but is not necessarily representative of the absolute flux uncertainty. For each extracted spectrum (i.e., from an aperture or spaxel), the ERR extension is rescaled such that the average value matches the RMS noise level of the data.

### 2.2 ALMA

The [C II] emission of this source has been observed by two ALMA projects (PI: M. Neeleman) using band 7 (Mahieu et al. 2012): 2015.1.01564.S ( $\sim 0.8''$  resolution) and 2017.1.01052.S ( $\sim 0.1''$  resolution). The resulting data have been well studied, including detailed kinematic analyses (see Neeleman et al. 2017, 2020; Jones et al. 2017, 2021; Roman-Oliveira et al. 2023). Here, we re-reduce the data in order to enable a fair comparison to our novel JWST/NIRSpec data.

The raw data for 2015.1.01564.S and 2017.1.01052.S were downloaded from the ALMA archive<sup>3</sup>, and were calibrated using the python scripts provided by ALMA staff in CASA (CASA Team et al. 2022) versions 4.5.1 and 5.1.1, respectively. We explored combining data from the two projects, but since the latter features both higher spatial resolution and a longer exposure time, we proceed using only the 2017.1.01052.S data. This project includes four spectral windows (SPWs): three containing only continuum emission (each with 128 channels of width 15.6250 MHz) and one containing continuum and [C II] emission (with 240 channels of width 7.8125 MHz).

An initial continuum map was created using the tclean task of CASA in multi-frequency synthesis (MFS) mode and natural weighting, excluding the SPW including [C II] emission. This map was then cleaned down to  $3\times$  the RMS noise level. This resulted in a synthesized beam of  $0.24'' \times 0.16''$  (PA  $-50^\circ$ ) and an RMS noise level of  $24 \mu\text{Jy/beam}$ .

Next, we subtracted the continuum emission underlying [C II] using the CASA task uvcontsub. This fit a first-order polynomial model to the visibilities of the three continuum SPWs, and subtracted an interpolation of this best-fit model from the SPW containing [C II]. The line-only visibilities were then imaged using tclean in ‘cube’ mode with natural weighting, with channels of  $25 \text{ km s}^{-1}$ . The resulting cube was cleaned down to  $3\times$  the RMS noise level. This resulted in a similar synthesized beam as the continuum map and an RMS noise level per channel of  $0.4 \text{ mJy/beam}$ .

## 3 SPECTRAL ANALYSIS

Our JWST/NIRSpec IFU observations were designed with the primary goal of detecting H $\alpha$  and using this strong line to measure the morpho-kinematics of the ionised gas in DLA0817g1. However, due to the wide spectral range of our R2700 data, we significantly detect additional emission lines. We perform a spaxel-by-spaxel fit of the H $\alpha$ -[N II] $\lambda$ 6548, 6584 complex in Section 3.1, a full fit of the integrated spectrum in Section 3.2, and determine ISM properties in Section 3.3.

### 3.1 Spatially resolved analysis

To begin, we extract a spectrum from each spaxel of our data cube and restrict the wavelength range to only contain emission from

<sup>1</sup> <https://ga-nifs.github.io/>

<sup>2</sup> <https://mast.stsci.edu/portal/Mashup/Clients/Mast/Portal.html>

<sup>3</sup> <https://almascience.eso.org/aq/>

[N II] $\lambda\lambda$ 6548, 6584 and H $\alpha$ <sup>4</sup>. In order to characterise the line emission, we fit each spectrum with a combined model containing continuum and line emission. The continuum is assumed to be a power law:

$$F_\lambda = F_{\text{cont}}(\lambda_{\text{obs}}/4\mu\text{m})^{\alpha_{\text{opt}}} \quad (1)$$

We assume that each line may be described as a single Gaussian component, and force the redshift and intrinsic linewidth (in velocity space;  $FWHM_V$ ) of all three lines to be equal. The line spread function (LSF<sup>5</sup>) is accounted for by adding the intrinsic linewidth and LSF in quadrature. The ratio between [N II] $\lambda$ 6548/[N II] $\lambda$ 6584 is derived using PYNEB (Luridiana et al. 2015), and we do not account for dust attenuation (see Section 3.3.2 for discussion of this assumption).

This model is fit to each spectrum using LMFIT (Newville et al. 2014). An initial fit is run with all parameters free, and the results are automatically inspected. Lines with insignificant emission ( $F_i < 3 \times \delta F_i$ , where  $\delta F_i$  is the reported flux uncertainty) are removed from the model. If the best-fit  $FWHM_V$  is very small ( $< 30 \text{ km s}^{-1}$ ), then the linewidth is set to be identical to the instrumental LSF.

We wish to compare these rest-optical morpho-kinematics to those of ALMA [C II] emission. Usually, ALMA moment maps are created using a non-parametric approach (i.e., the CASA task IMMOMENTS; e.g., Harikane et al. 2020; Gururajan et al. 2022; Rowland et al. 2024). In order to ensure a fair comparison, we fit the ALMA [C II] cube in a similar fashion to the NIRSPEC IFU data. Specifically, we fit the spectrum of each spaxel in the continuum-subtracted [C II] data cube (see Section 2.2) using a single Gaussian model. Since we are interested in comparing the morpho-kinematics of [C II] and H $\alpha$  rather than any rest-optical to rest-FIR line ratios, we keep the ALMA data in its native units.

The resulting line flux maps (Figure 1) show strong emission from DLA0817g1 in H $\alpha$ , [N II] $\lambda$ 6584, and [C II]. The distribution of H $\alpha$  and [C II] are similar, but feature a slight spatial offset between the peak values (rightmost panel). To quantify this, we use PYSERSIC (Pasha & Miller 2023) to fit the H $\alpha$  and [C II] morphology of DLA0817g1 while accounting for the different PSF shapes. The resulting best-fit properties (listed in Table 1) show remarkable agreement between the two line tracers, with ellipticity (defined as  $1 - (b/a)$ ) of  $\sim 0.3$ , Sérsic index  $\sim 0.9$ , position angle  $\sim 82^\circ$ , and effective radius  $\sim 2 \text{ kpc}$ .

From the PYSERSIC fits, we find that the spatial centroids of the [C II] and H $\alpha$  distributions are offset by  $62 \pm 18 \text{ mas}$  (where the uncertainty includes both the reported uncertainty in each fit and the astrometric uncertainties derived in Appendix A), corresponding to a physical offset of  $0.42 \pm 0.12 \text{ kpc}$ . But as we will discuss in Section 4, this apparent offset (and its significance) are likely due to the assumption of a radially symmetric model and under-predicted uncertainties.

Based on the best fit to the H $\alpha$  data, we calculate a half-light aperture with the same axis ratio and position angle as the Sérsic profile, but that encloses 50% of the total flux. We then define an aperture with axes of  $1.25\times$  that of the half-light profile (enclosing

<sup>4</sup> Detailed spatial analysis of the other lines and the continuum will be performed in other works (e.g., using the JWST/NIRSpec IFU G395M/F290LP data of PID 5761, PI Neeleman), and here we are primarily interested in the morpho-kinematics of H $\alpha$ .

<sup>5</sup> We determine the LSF using the fiducial resolving power curves recorded at <https://jwst-docs.stsci.edu/jwst-near-infrared-spectrograph/nirspec-instrumentation/nirspec-dispersers-and-filters>.

Property	H $\alpha$	[C II]
Ellipticity	$0.29 \pm 0.02$	$0.26 \pm 0.04$
$n_s$	$0.9 \pm 0.1$	$0.8 \pm 0.1$
PA [ $^\circ$ ]	$82 \pm 2$	$89 \pm 12$
$R_e$ ["]	$0.29 \pm 0.01$	$0.28 \pm 0.01$
$R_e$ [kpc]	$2.0 \pm 0.1$	$1.9 \pm 0.1$

**Table 1.** Best-fit morphological properties of the H $\alpha$  and [C II] emission, as derived through PYSERSIC fits.

$\sim 60\%$  of the flux), which is shown in each figure as a white ellipse, and will be used in the next subsection to extract a total spectrum.

To examine the kinematics of this source, we create maps of  $v_{50}$ <sup>6</sup> and  $w_{80} \equiv v_{90} - v_{10}$ . Since we are using Gaussian profiles,  $v_{50}$  is the best-fit velocity offset of the line centroid from an assumed redshift of  $z = 4.2603$ , while  $w_{80} \simeq 1.088\times$  the Gaussian FWHM. The kinematic maps (Figure 2) show similar behaviour between the two tracers, which we further explore in Sections 4 and 5.1.

### 3.2 Integrated spectral analysis

Next, we take a detailed look at the galaxy as a whole by extracting an integrated spectrum from our data cube using the aperture defined in the previous subsection (see Figure 3). An aperture loss correction is derived by calculating the ratio of the best-fit H $\alpha$  Sérsic profile inside the aperture to the total flux (i.e.,  $\sim 1.6\times$ ). Both the continuum (Equation 1) and emission lines (HeI $\lambda$ 5875, [N II] $\lambda\lambda$ 6548, 6584, H $\alpha$ , [S II] $\lambda\lambda$ 6716, 6731, and [S III] $\lambda\lambda$ 9069, 9532) are included in each fit. First, we explore the possibility that each line can be described by a single Gaussian profile ('1G' in Table 2), where the kinematics of each line are tied. But since this results in significant residuals in the fit of H $\alpha$  (Figure 3), we instead model each line as a combination of two Gaussians (2G<sub>red</sub> and 2G<sub>blue</sub>), each with its own redshift and intrinsic (i.e., LSF-corrected) linewidth. We note that while this approach is a simple approximation of the morpho-kinematics of the source, the resulting residuals are low, and the model returns a lower reduced  $\chi^2$  than the single-Gaussian model. A full dynamical analysis of these data are presented in Section 4.

The flux of each line is set to be independent, in order to explore ISM conditions. Lines are assumed to lie at the same redshift. The resulting fits to each spectral line are shown in Figure 3, while the resulting best-fit values are listed in Table 2.

### 3.3 Resulting ISM properties

#### 3.3.1 Electron density

We may use the density-dependent ratio [S II] $\lambda$ 6716/[S II] $\lambda$ 6731 ratio to find the electron density  $n_e$  through the PYNEB task *getTemDen*. Assuming  $T_e = 1.3 \times 10^4 \text{ K}$  (see Section 3.3.2), we estimate  $\log_{10}(n_e[\text{cm}^{-3}]) = 2.5 \pm 0.4$ . This value is in agreement with the expected value at  $z = 4.2603$  from other works (e.g., Isobe et al. 2023; Li et al. 2025a,b). As shown in Table 3, this property is not significantly affected by dust extinction due to the close spacing of the [S II] $\lambda\lambda$ 6716, 6731 doublet.

<sup>6</sup> We use the notation  $v_N$  to represent the velocity where  $N\%$  of the line flux lies between  $-\infty < v < v_N$ .



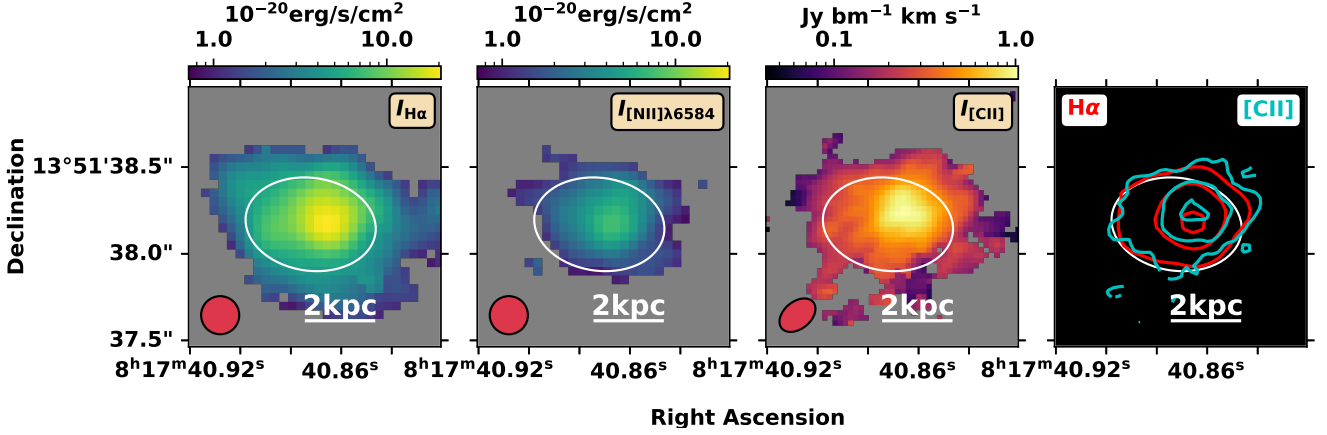


**Figure 1.** Best fit line intensity maps of  $H\alpha$ ,  $[N II]\lambda 6584$ , and  $[C II]$ , where values are given per pixel. In the rightmost panel, we instead compare the  $H\alpha$  (red) and  $[C II]$  (cyan) emission using contours of  $[0.25, 0.50, 0.90] \times$  the peak value of each. In each panel, we show a physical scale of 2 kpc. The PSF is represented as a red circle or ellipse to the southeast (north is up and east is to the left). Our adopted aperture is shown as a white ellipse.

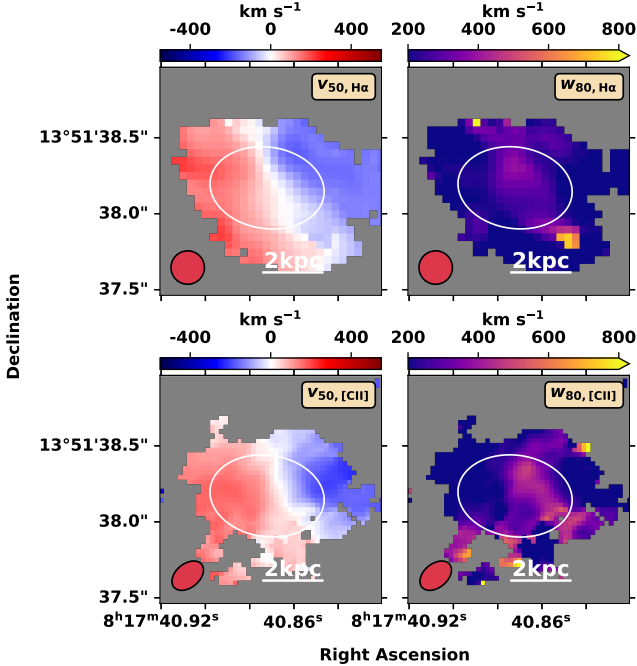


**Figure 2.** Best fit  $v_{50}$  (left column) and  $w_{80}$  (right column) maps for  $H\alpha$  (top row) and  $[C II]$  (lower row). In each panel, we show a physical scale of 2 kpc. The PSF is represented as a red circle or ellipse to the southeast (north is up and east is to the left). Our adopted aperture is shown as a white ellipse.

### 3.3.2 Dust attenuation and electron temperature

It is now common to explore the dust attenuation of high-redshift galaxies with JWST by measuring multiple strong Balmer emission lines (e.g.,  $H\alpha$  and  $H\beta$ ) and determine the dust attenuation (parametrised as  $E(B - V)$  or  $A_V$ ) by comparing their intrinsic and observed flux ratios (assuming a dust attenuation curve; e.g., Calzetti et al. 2000). Since only one Balmer line falls within our spectral coverage, we explore two avenues to constrain the dust attenuation. First, we explore a prelimi-

Property	Model	Value	Units
$z$	1G	$4.2606 \pm 0.0001$	
	2G <sub>blue</sub>	$4.2579 \pm 0.0003$	
	2G <sub>red</sub>	$4.2618 \pm 0.0002$	
$FWHM_V$	1G	$366 \pm 6$	$[km s^{-1}]$
	2G <sub>blue</sub>	$182 \pm 25$	$[km s^{-1}]$
	2G <sub>red</sub>	$241 \pm 20$	$[km s^{-1}]$
$F_{H\alpha}$		$2033.84 \pm 198.85$	$[10^{-20} \text{ erg s}^{-1} \text{ cm}^{-2}]$
$F_{[NII]\lambda 6584}$		$692.29 \pm 29.79$	$[10^{-20} \text{ erg s}^{-1} \text{ cm}^{-2}]$
$F_{[NII]\lambda 6716}$		$337.78 \pm 42.42$	$[10^{-20} \text{ erg s}^{-1} \text{ cm}^{-2}]$
$F_{[NII]\lambda 6731}$		$227.21 \pm 42.42$	$[10^{-20} \text{ erg s}^{-1} \text{ cm}^{-2}]$
$F_{[SIII]\lambda 9069}$		$187.47 \pm 32.77$	$[10^{-20} \text{ erg s}^{-1} \text{ cm}^{-2}]$
$F_{[SII]\lambda 9532}$		$558.80 \pm 32.77$	$[10^{-20} \text{ erg s}^{-1} \text{ cm}^{-2}]$
$F_{cont}$		$1.46 \pm 0.03$	$[10^{-20} \text{ erg s}^{-1} \text{ cm}^{-2} \text{ \AA}^{-1}]$
$\alpha_{opt}$		$-1.47 \pm 0.10$	$[10^{-20} \text{ erg s}^{-1} \text{ cm}^{-2} \text{ \AA}^{-1}]$

**Table 2.** Best-fit quantities of DLA0817g1, as derived from fits to the integrated spectrum. For the redshift and intrinsic width of each lines (i.e., accounting for the LSF), we list the results for the single Gaussian model (1G) and the two components of the double Gaussian model (2G<sub>red</sub> and 2G<sub>red</sub>). The line fluxes are the total values from the double Gaussian model. No dust correction has been applied.

nary constraint on the dust attenuation through the our observed  $[N II]\lambda 6548/[N II]\lambda 6584$  and  $[S III]\lambda 9069/[S III]\lambda 9532$  ratios (which are independent of ISM conditions:  $[N II]\lambda 6548/[N II]\lambda 6584 = 0.340$  and  $[S III]\lambda 9069/[S III]\lambda 9532 = 0.405$ ).

As shown in Figure 4, we explore a range of  $0 \leq E(B - V) \leq 10$ , redden each of the intrinsic line ratios (red line; as derived with PYNEB), and compare them to our observed line ratios and the associated uncertainties (black line and shaded region; see Table 2). Due to the large fitting uncertainties in each observed ratio, there is no definite value of  $E(B - V)$  that is preferred by our data. The observed  $[N II]\lambda 6548/[N II]\lambda 6584 = 0.33 \pm 0.05$  is well described by any colour excess in our explored range (due to the small wavelength separation of the two lines), while the  $[S III]\lambda 9069/[S III]\lambda 9532 = 0.34 \pm 0.06$

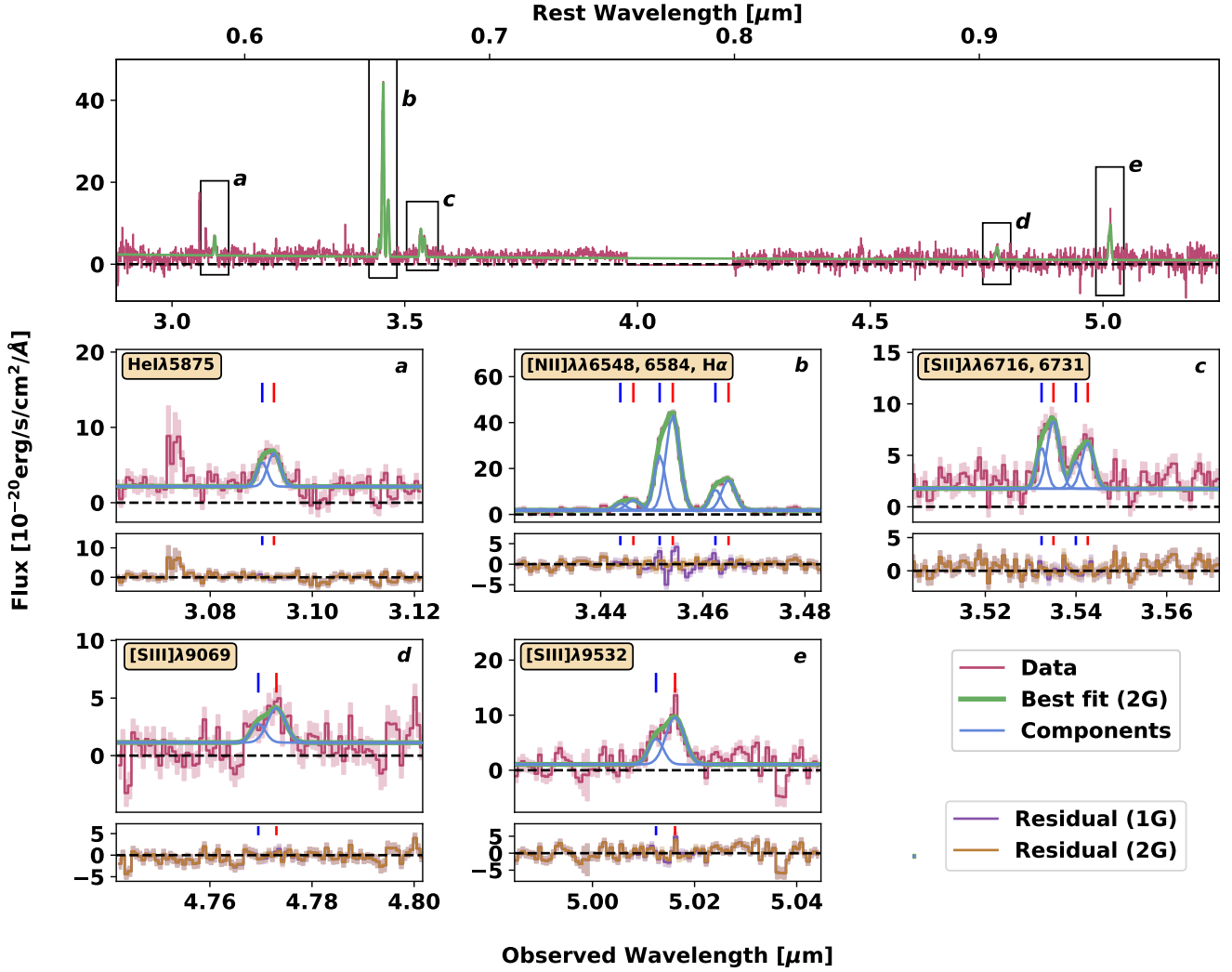


**Figure 3.** Results of fitting integrated spectrum of DLA0817g1. The top panel shows a full spectrum (pink line with  $1\sigma$  uncertainty shown as shaded region) along with the best-fit model (green). Panels a-e are zoomed-in views for each line, showing the individual best-fit Gaussian components (light blue) and the centroid wavelength of each of the 2-Gaussian fits (red and blue lines above each spectrum). The lower portion of each panel depicts the residual spectra for a single-Gaussian fit (purple) and out two-Gaussian fit (brown).

Property	$E(B - V) = 0$	$E(B - V) = 0.4$	Units
$\log_{10}(S2)$	$-0.56 \pm 0.06$	$-0.57 \pm 0.06$	-
$\log_{10}(S3)$	$-0.44 \pm 0.05$	$-0.64 \pm 0.05$	-
$\log_{10}(S23)$	$-0.19 \pm 0.05$	$-0.30 \pm 0.05$	-
$\log_{10}(S32)$	$0.12 \pm 0.05$	$-0.07 \pm 0.05$	-
$\log_{10}(N2)$	$-0.47 \pm 0.05$	$-0.47 \pm 0.05$	-
$\log_{10}(N2S2)$	$0.09 \pm 0.05$	$0.10 \pm 0.05$	-
$\log_{10}(n_e [\text{cm}^{-3}])$	$2.47 \pm 0.43$	$2.45 \pm 0.40$	-
$12 + \log_{10}(O/H)$	$8.52 \pm 0.07$	$8.54 \pm 0.09$	-
$Z$	$0.68 \pm 0.11$	$0.70 \pm 0.14$	$[Z_{\odot}]$
$SFR_{H\alpha}$	$17 \pm 1$	$59 \pm 5$	$[M_{\odot} \text{ yr}^{-1}]$
$\log_{10}(U)$	$-3.43 \pm 0.06$	$-3.64 \pm 0.06$	-
$\alpha_{[CII]}(Z)$	$5.45 \pm 0.34$	$5.38 \pm 0.41$	$[M_{\odot} L_{\odot}^{-1}]$
$\log_{10}(M_{H_2, [CII]} [M_{\odot}])$	$10.25 \pm 0.04$	$10.24 \pm 0.04$	-

**Table 3.** Derived properties of DLA0817g1, as derived from a spectral fit to the integrated spectrum. For each, we present both the observed value ( $E(B - V) = 0$ ) and a value corrected for the estimated dust attenuation ( $E(B - V) = 0.4$ ), see Section 3.3.2

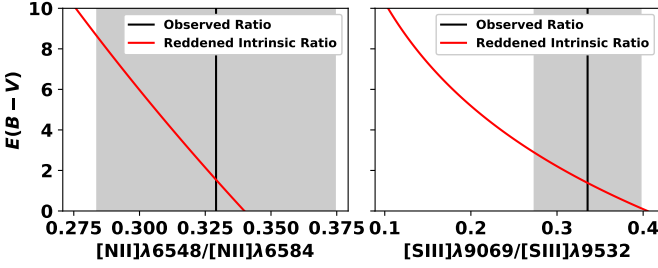


**Figure 4.** Preliminary test to constrain  $E(B - V)$  from our observed  $[\text{N II}]\lambda 6548, 6584$  and  $[\text{S III}]\lambda 9069, 9532$  ratios. For each panel, we show the observed ratio and its  $1\sigma$  uncertainty as a black line and shaded region, respectively. The dust-reddened intrinsic value of each ratio for a given  $E(B - V)$  is shown as a red dashed line.

appears to argue for  $E(B - V) \lesssim 3$ . This limit excludes the extreme case of hot dust-obscured galaxies, which can feature  $E(B - V) > 10$  (e.g., Assef et al. 2016), but encompasses the range of most JWST-derived values for  $z > 4$  galaxies ( $E(B - V) \lesssim 1$ ; e.g., Fujimoto et al. 2025; Jones et al. 2024; Navarro-Carrera et al. 2025; Kiyota et al. 2025).

As an alternative, we collect the fluxes of our detected lines and the upper limits of our undetected lines<sup>7</sup> and use a Bayesian inference approach (ULTRANEST) to simultaneously constrain  $T_e$  and  $E(B - V)$  through comparisons to PYNEB models.

Specifically, we adopt the best-fit  $n_e$  value from our  $[\text{S II}]\lambda 6716, 6731$  ratio (which is not strongly affected by temperature or dust attenuation), a log-uniform prior of  $0.5 < T_e/10^4 \text{ K} < 2.4$ , and a uniform prior of  $0 < E(B - V) < 5$ . We use PYNEB to calculate the expected line ratio  $\mathcal{R}_x$  given a set of input parameters  $x = \{n_e, T_e, E(B - V)\}$ . For each observed line ratio ( $R_i \pm \delta R_i$ ), the likelihood is (e.g., Kerrison et al. 2024; Whitler et al. 2025):

$$\mathcal{L}_i = \frac{1}{\sqrt{2\pi}\delta R_i} \exp\left(-\frac{(\mathcal{R}_x - R_i)^2}{2\delta R_i^2}\right) \quad (2)$$

For non-detections, we calculate the likelihood given the  $3\sigma$  upper limit ( $< 3\delta R_j$ ):

$$\mathcal{L}_j = 0.5 \times \text{erfc}\left(\frac{\mathcal{R}_x - 3\delta R_j}{\sqrt{2}\delta R_j}\right) \quad (3)$$

The total likelihood for  $N_D$  detected ratios ( $[\text{N II}]\lambda 6548/[\text{N II}]\lambda 6584$ ,  $[\text{S II}]\lambda 6716/[\text{S II}]\lambda 6731$ ,  $[\text{S III}]\lambda 9069/[\text{S III}]\lambda 9532$ ) and  $N_U$  upper limits on ratios (including the detected lines listed in Table 2 and upper limits on  $[\text{N II}]\lambda 5755$ ,  $[\text{S III}]\lambda 6312$ ,  $\text{He I}\lambda 6678$ ,  $\text{He I}\lambda 7065$ ,  $\text{H I}\lambda 9014$ ,  $\text{H I}\lambda 9546$ , and  $\text{H I}\lambda 9229$ ) is then given as:

$$\mathcal{L}_{\text{total}} = \prod_i^{N_D} \mathcal{L}_i \prod_j^{N_U} \mathcal{L}_j \quad (4)$$

Using ULTRANEST with the above priors and likelihood function, we find best-fit values of  $T_e = (1.2^{+0.7}_{-0.5}) \times 10^4 \text{ K}$  and  $E(B - V) = 0.4^{+0.5}_{-0.3}$  (giving the 16, 50, and 84% percentile locations). When combined with the posterior distribution shapes (which are peaked in the lowest explored bin, see Figure C1), this suggests a low dust attenuation and

<sup>7</sup> Upper limits on line fluxes are calculated by creating 1000 mock spectra with the same noise level as the data, adding mock lines (adopting the kinematics of the  $\text{H}\alpha$  line) with different fluxes, and finding the flux limit where we recover the line 68% of the time.

Name	Ratio
S2	$[\text{S II}]\lambda 6716, 6731/\text{H}\alpha$
S3	$[\text{S III}]\lambda 9069, 9532/\text{H}\alpha$
S23	$([\text{S II}]\lambda 6716, 6731 + [\text{S III}]\lambda 9069, 9532)/\text{H}\alpha$
S32	$[\text{S III}]\lambda 9069, 9532/[\text{S II}]\lambda 6716, 6731$
N2	$[\text{N II}]\lambda 6584/\text{H}\alpha$
N2S2	$[\text{N II}]\lambda 6584/[\text{S II}]\lambda 6716, 6731$

**Table 4.** Definitions of line ratios used in this work (e.g., Sanders et al. 2025).

a cold temperature. Further observations (e.g.,  $\text{H}\beta$ ,  $\text{O II}\lambda 3726, 3729$ ) are needed to better constrain these properties. For the rest of this Section, we present results assuming  $T_e = 1.2 \times 10^4 \text{ K}$  and both the observed quantities with no dust correction ( $E(B - V) = 0$ ) and a dust correction of  $E(B - V) = 0.4$  (see Table 3).

### 3.3.3 Line ratios and metallicities

Our observed emission lines open a powerful window into the properties of DLA0817g1 through the use of line ratio diagnostics. The gas-phase metallicities are derived by applying the diagnostics of Sanders et al. (2025) to the line ratios listed in Table 4. Specifically, we use the chi-squared minimization approach of Curti et al. (2020, see their equation 1). These results are given in solar units, assuming a solar metallicity of  $12 + \log(O/H) = 8.69$  (Allende Prieto et al. 2001). We find that ratios with closely spaced lines (e.g., S2, N2) are not strongly affected by dust attenuation, while  $> 3\sigma$  differences are seen in ratios of distant lines (e.g., S3, S32). Despite this, the best-fit metallicity ( $0.7 \pm 0.2$  solar) is similar for both dust correction cases.

### 3.3.4 Star formation rate

Next, we infer the star formation rate (SFR) using the best-fit dust-corrected  $\text{H}\alpha$  flux. Using PYNEB, we estimate the attenuation-free ratio of  $\text{H}\alpha/\text{H}\beta$ . Combining this with the calibration of Kennicutt (1998) yields:

$$\frac{SFR_{\text{H}\alpha}}{[M_\odot \text{ yr}^{-1}]} = \frac{4\pi C_{\text{SFR}} F_{\text{H}\alpha}}{[erg \text{ s}^{-1} \text{ cm}^{-2}]} \left(\frac{D_L}{[cm]}\right)^2 \frac{[erg \text{ s}^{-1} M_\odot^{-1} \text{ yr}]}{1.26 \times 10^{41}} \quad (5)$$

where the factor of  $C_{\text{SFR}}$  is included to convert from a Salpeter (1955) IMF to a Chabrier (2003) IMF. Previous works used a range of  $C_{\text{SFR}} \sim 0.56 - 0.65$  (e.g., Panter et al. 2007; Longhetti & Saracco 2009; Dutton et al. 2010; González et al. 2010; Béthermin et al. 2012; Driver et al. 2013; Madau & Dickinson 2014; Caputi et al. 2017; Figueira et al. 2022; Hsiao et al. 2024b). We briefly note that some recent investigations of high redshift galaxies ( $z > 6$ ) with JWST have instead used conversion factors based on stellar population synthesis models (Reddy et al. 2018, 2022). These models, which assume a low metallicity, result in lower factors (e.g.,  $C_{\text{SFR}} = 0.27$ ; Saxena et al. 2023; Curti et al. 2024,  $C_{\text{SFR}} \sim 0.40$ ; Hsiao et al. 2024a). In this work, we adopt a Chabrier (2003) IMF and  $C_{\text{SFR}} \sim 0.61$ , as in another high-redshift JWST work (Hsiao et al. 2024b).

We find  $SFR_{\text{H}\alpha} = 17 \pm 1 M_\odot \text{ yr}^{-1}$  for the case of no dust correction, and  $SFR_{\text{H}\alpha} = 59 \pm 5 M_\odot \text{ yr}^{-1}$  for the case of  $E(B - V) = 0.4$ . The dust-free case is  $< 1\sigma$  discrepant from the  $SFR_{\text{NUV}} = 16 \pm 3 M_\odot \text{ yr}^{-1}$  found by Neeleman et al. (2020), while even the dust-corrected value is smaller than the FIR-based  $SFR_{160\mu\text{m}} = 118 \pm 14 M_\odot \text{ yr}^{-1}$ . This suggests a considerable fraction of obscured star formation. While a high  $SFR_{[\text{CII}]}$  =  $420 \pm 260 M_\odot \text{ yr}^{-1}$  value is reported by Neeleman et al. (2020), the low significance ( $< 3\sigma$ ) makes it difficult to compare.

### 3.3.5 Ionisation parameter

We estimate the ionisation parameter  $U$  using a relation of Kewley et al. (2019), which is dependent on S32, metallicity, and ISM pressure ( $P_{\text{ISM}}$ ), parametrised as  $\log_{10}(P_{\text{ISM}}/k_B)$  ( $k_B$  is the Boltzmann constant). Using our best-fit S32 and metallicity, we find that the high-pressure ( $\log_{10}(P_{\text{ISM}}/k_B) = 7$ ) and low pressure ( $\log_{10}(P_{\text{ISM}}/k_B) = 5$ ) diagnostics return similar  $\log_{10}(U)$  values (i.e.,  $< 1\sigma$  discrepant), and adopt the high-pressure case. The S32 values and resulting ionisation parameters ( $\log_{10}(U) = -3.43$  to  $-3.64$ ) lie at the weak edge of the distribution of high-redshift values (e.g., Reddy et al. 2023; Shapley et al. 2025).

### 3.3.6 WHAN diagram

Due to our spectral setup, we lack the wavelength coverage necessary to study the placement of DLA0817g1 on several common line ratio diagnostic diagrams that differentiate between excitation by AGN and star formation (e.g., BPT Baldwin et al. 1981, VO-87 Veilleux & Osterbrock 1987, R3O1 Kewley et al. 2001). However, our high spectral resolution and strong detections of  $H\alpha$  and  $[\text{N II}]\lambda 6584$  enable the use of the equivalent width of  $H\alpha$  vs.  $[\text{N II}]/H\alpha$  (WHAN; Cid Fernandes et al. 2010, 2011) diagram.

The WHAN diagram has been applied to other  $z > 4$  galaxies, including the JWST/NIRSpec IFU observations of GN20 from GANIFS (Übler et al. 2024). This previous analysis showed that the majority of the spaxels are classified as strong AGN (or ‘Seyfert-like’), while some spaxels on the outskirts are instead classified as likely star-forming. Similarly, D’Eugenio et al. (2025) use this diagnostic to classify the  $z = 4.6348$  galaxy Ulema as an AGN.

In the top panel of Figure 5, we show the location of each spaxel-based spectrum in the WHAN diagnostic plot. All of the points for DLA0817g1 meet the  $\log_{10}(EW_{H\alpha}[\text{\AA}]) > 0.5$  criterion necessary to rule out classification as a passive or retired galaxy (and could be higher in the case of significant dust attenuation; see Section 3.3.2), and nearly all of the spaxels meet the  $\log_{10}(\text{N2}) < -0.4$  criterion for excitation by star formation rather than an AGN (green points). To investigate the few spaxels that lie in the ‘strong AGN’ regime of this diagnostic (yellow points), we show the spatial distribution of spaxel-by-spaxel WHAN classification in the bottom panel of Figure 5. The high-N2 points (shown as black stars) lie in the outskirts of the galaxy, and are likely affected by a lower-significance  $[\text{N II}]\lambda 6584$  detection. While this suggests that DLA0817g1 is likely excited by star formation, further observations will enable tests to search for the presence of an AGN (e.g., the additional diagnostic plots of Mazzolari et al. 2024, the WHaO diagnostic of Sánchez et al. 2025) are required to confirm the presence or absence of an AGN.

## 4 TILTED RING MODELS

### 4.1 Overview

Previous studies of the  $[\text{C II}]$  emission of DLA0817g1 showed evidence for a regular rotating galaxy. Our new JWST/NIRSpec IFU data allow us to perform a similar analysis of the ionised gas, using  $H\alpha$  as a kinematic tracer. To do this, we use the tilted ring fitting code <sup>3D</sup>Barolo (Di Teodoro & Fraternali 2015) to perform a parallel analysis of the  $[\text{C II}]$  and  $H\alpha$  data cubes. In this way, we can compare the molecular and ionised gas morpho-kinematics in a similar fashion.

As a tilted ring fitter, <sup>3D</sup>Barolo works by decomposing the morphokinematics of a galaxy into a set of rings with independent prop-

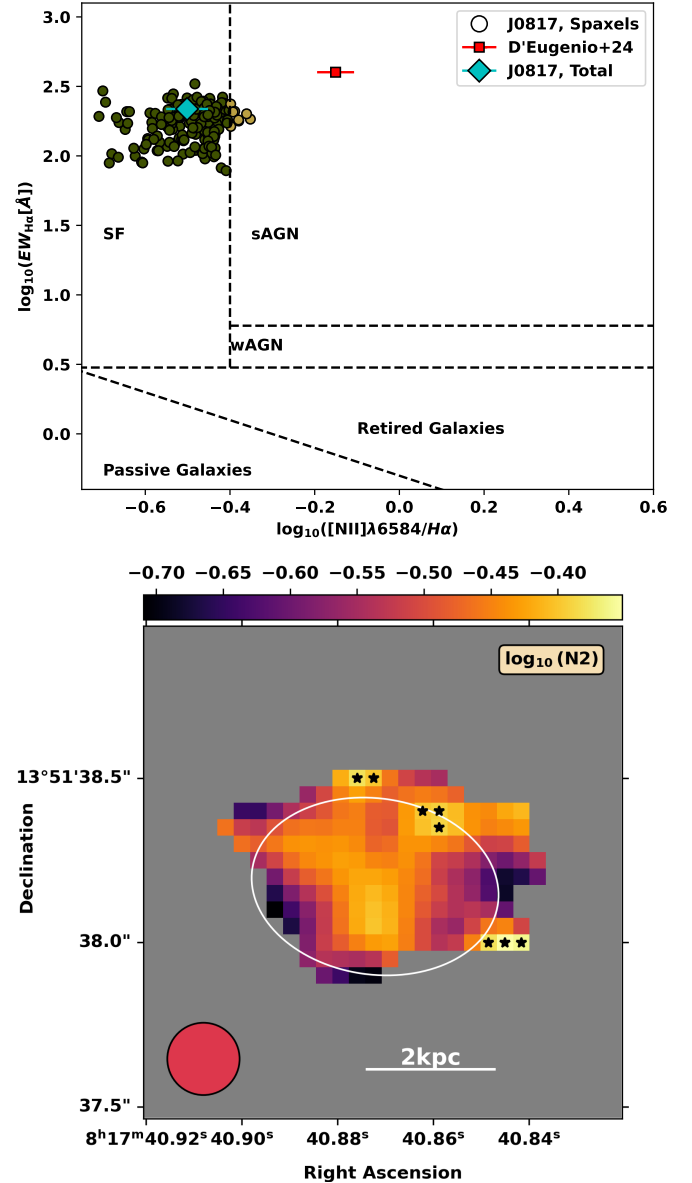


**Figure 5.** Results of WHAN diagnostics. The top panel shows the distribution of spaxel values in the  $\log_{10}(EW_{H\alpha}/AA)$ - $\log_{10}(\text{N2})$  space, with the demarcation lines and classifications of Cid Fernandes et al. (2010) included. The circles and blue diamond show the values found through a fit to the spaxel-by-spaxel spectra and the integrated spectrum, respectively. For comparison, we also show the location of a  $z = 4.6348$  AGN host galaxy studied with JWST/NIRSpec (red point - Ulema; D’Eugenio et al. 2025). In the bottom panel, we show the spatial distribution of  $\log_{10}(\text{N2})$  (i.e., the x-axis of the upper panel), with spaxels that would be classified as ‘strong AGN’ marked with black stars (and all other coloured spaxels classified as ‘SF’). The PSF is represented as a red circle to the southeast (north is up and east is to the left), and we include a physical scale of 2 kpc. Our adopted aperture is shown as the white ellipse.

erties. This code takes as input the desired ring width, ring height, and the number of rings desired. The user provides a set of initial estimates for the morphological (i.e., central position, inclination, position angle, brightness) and kinematic parameters (i.e., rotational velocity, velocity dispersion) for each ring. The code then creates a three-dimensional cube with spatial axes, and populates the cube



with gas particles by sampling from the input parameters from each ring. This physical model is converted to an observation-like data cube, with the same geometry as the observed data cube (i.e., right ascension, declination, and velocity). At this point, the mock data are convolved with the PSF (or synthesised beam for interferometric observations) of the observations. The model flux is normalised by comparison to the observed data cube. This allows the data and model cubes to be compared on a pixel-by-pixel basis.

## 4.2 Implementation

Due to its fitting approach, <sup>3D</sup>Barolo fits for the geometric and kinematic properties of a galaxy simultaneously. Here, we describe the assumptions that go into our modelling.

First, we assume that the galaxy may be modelled by a thin disk with a Gaussian vertical mass distribution (scale height  $0.01''$ ) with maximum radius  $r = 3.5$  kpc (e.g., [Neeleman et al. 2020](#)). The ring width is calculated by dividing the FWHM of the minor axis of the PSF (or synthesised beam for ALMA) by 1.5, a conservative middle ground between the values from high-redshift ( $\gtrsim 2$ ; e.g., [Shao et al. 2017](#); [Talia et al. 2018](#); [Fan et al. 2019](#); [Jones et al. 2020](#)) and low-redshift studies ( $\lesssim 1$ ; e.g., [Shelest & Lelli 2020](#); [Mancera Piña et al. 2020](#); [Salak et al. 2020](#)). This results in five  $0.10''$ -wide rings for the [C II] data and four  $0.13''$ -wide rings for the H $\alpha$  data.

Because <sup>3D</sup>Barolo compares the data and model directly, it is vital to first mask the input data cube, to avoid fitting a model to noise. We do this by using the <sup>3D</sup>Barolo task `SEARCH`, which searches each data cube for emission above some high threshold (which we set to  $5\times$  the RMS noise level of the cube) and creates a mask by expanding these regions in both the spatial and spectral directions until it encounters emission lower than a given threshold (which we set to  $2\times$  the RMS noise level). We apply this mask to our data.

Using the channels that were identified as including signal, we create a moment 0 map (CASA `IMMOMENTS`) and fit a 2D Gaussian to the resulting emission. The best-fit spatial centroid and position angle are input to <sup>3D</sup>Barolo as initial estimates. We assume that the intrinsic galaxy is circular and use the ratio of the best-fit FWHMs of the semi-major axes (which are PSF-corrected) to estimate the inclination. The inclination and position angle are allowed to vary by  $\pm 20^\circ$  and  $\pm 15^\circ$  from these initial estimates, respectively. More sophisticated methods of deriving the morphological parameters exist (e.g.; `CANNUBI`, [Roman-Oliveira et al. 2023](#)), but due to the high signal to noise of our data, our approach results in precise constraints.

The initial estimate of the systemic redshift is  $z = 4.2603$ . We provide a constant rotational velocity estimate for all rings of  $10^2$  km s<sup>-1</sup>, and constrain this value to be  $< 10^3$  km s<sup>-1</sup>. To estimate the velocity dispersion, we create a moment 2 map (CASA `IMMOMENTS`) using the emission identified through <sup>3D</sup>Barolo `SEARCH` and measure the central value. Again, we limit this value to  $< 10^3$  km s<sup>-1</sup>. Our model does not include any radial motion.

We first perform an initial tilted ring model fit by allowing all parameters for each ring (i.e., rotational velocity, velocity dispersion, inclination, position angle, systemic velocity) to be free. The resulting morphological parameters (which will vary from ring to ring) are then smoothed with a Bezier function, and a second fit is performed where the morphology of the galaxy is fixed.

Throughout the fitting procedure, we fit both sides of the disk simultaneously and apply uniform weighting to all azimuthal angles. The model is normalised on a pixel-by-pixel basis such that the integrated intensity matches that of the masked cube.

Property	H $\alpha$	[C II]
$i_{\text{morph}} [^\circ]$	$46 \pm 2$	$46 \pm 6$
$i_{\text{kin}} [^\circ]$	$51 \pm 6$	$60 \pm 3$
$PA_{\text{morph}} [^\circ]$	$87 \pm 2$	$106 \pm 10$
$PA_{\text{kin}} [^\circ]$	$113 \pm 8$	$109 \pm 9$
$v_{\text{rot}}(R_e)$ [km s <sup>-1</sup> ]	$206 \pm 14$	$235 \pm 16$
$\sigma_o(R_e)$ [km s <sup>-1</sup> ]	$97 \pm 12$	$49 \pm 11$
$v_{\text{rot}}(R_e)/\sigma_o(R_e)$	$2.1 \pm 0.3$	$4.8 \pm 1.1$
$\log_{10}(M_{\text{dyn}}/M_\odot)$	$10.9 \pm 0.1$	$10.8 \pm 0.1$

**Table 5.** Best-fit morpho-kinematic properties of the H $\alpha$  and [C II] emission, as derived through our <sup>3D</sup>Barolo fits.

## 4.3 Results

The results of this second fit are inspected by comparing the data and model cubes in multiple ways, which we display in Figure 6. First, we consider the integrated intensity (moment 0; M0), line-of-sight velocity (moment 1; M1), and velocity dispersion (moment 2; M2) maps, which we create using the CASA task `IMMOMENTS`. Next, we use the best-fit position angle to define the kinematic major and minor axes, and extract position-velocity diagrams (PVDs) along both. The best-fit morphological and kinematic properties are listed in Table 5.

From Figure 6, it is clear that the morphology and kinematics are similar between the [C II] and H $\alpha$  data (as already seen in Section 3.1), with a strong east-west velocity gradient (M1) and coincident peaks of intensity and velocity dispersion (M0 and M2, respectively). The <sup>3D</sup>Barolo models fit these data well, with the M1 residuals showing only minor features. One significant difference between the datasets is the velocity resolution, which can be seen in the spectrally-resolved major axis PVD of the [C II] data and the coarser PVD of the H $\alpha$  data. While all of the panels in Figure 6 include observational effects (e.g., synthesised beam or PSF smearing, spectral and spatial binning), we may also compare the best-fit parameters directly.

One of the primary ways that we may compare the <sup>3D</sup>Barolo fits is to plot the best-fit curves of rotation velocity, velocity dispersion, and the ratio of the two. The top left panel of Figure 7 shows a remarkable agreement between the best-fit rotation curves of the two datasets, despite the fact that the modelling was done separately (i.e., without linked priors). On the other hand, the velocity dispersion of H $\alpha$  is about twice that of [C II] (central left panel), resulting in a higher degree of rotational support based on the [C II] data (lower left panel). This apparent discrepancy originates from the different phases probed by the two emission lines: molecular gas for [C II] and ionised gas for H $\alpha$ . Observations and simulations have demonstrated that while ionised and molecular gas kinematics trace the same rotation profile, the velocity dispersion of ionised gas is  $\sim 2 - 3$  that of molecular gas (e.g., [Fujimoto et al. 2025](#); [Kohandel et al. 2024](#); [Parlanti et al. 2024](#); [Rizzo et al. 2024](#); see discussion in Section 5.1).

From these fits, we find that the best-fit spatial centroids of the [C II] and H $\alpha$  data show no significant offset ( $18 \pm 170$  mas, where the uncertainty includes both the reported uncertainty in each fit and the astrometric uncertainties derived in Appendix A). At face value, this appears to contradict the  $\sim 4\sigma$  spatial offset between the best-fit centroids from the `PYSERSIC` fit of Section 3.1. While the emission is well approximated by a Sérsic profile, it is clear from Figure 1 and 6 that there are deviations from radial symmetry which complicate the fit of such a profile. In addition, we perform the `PYSERSIC` fits on spatially masked data, resulting in biased uncertainty estimates. Thus,

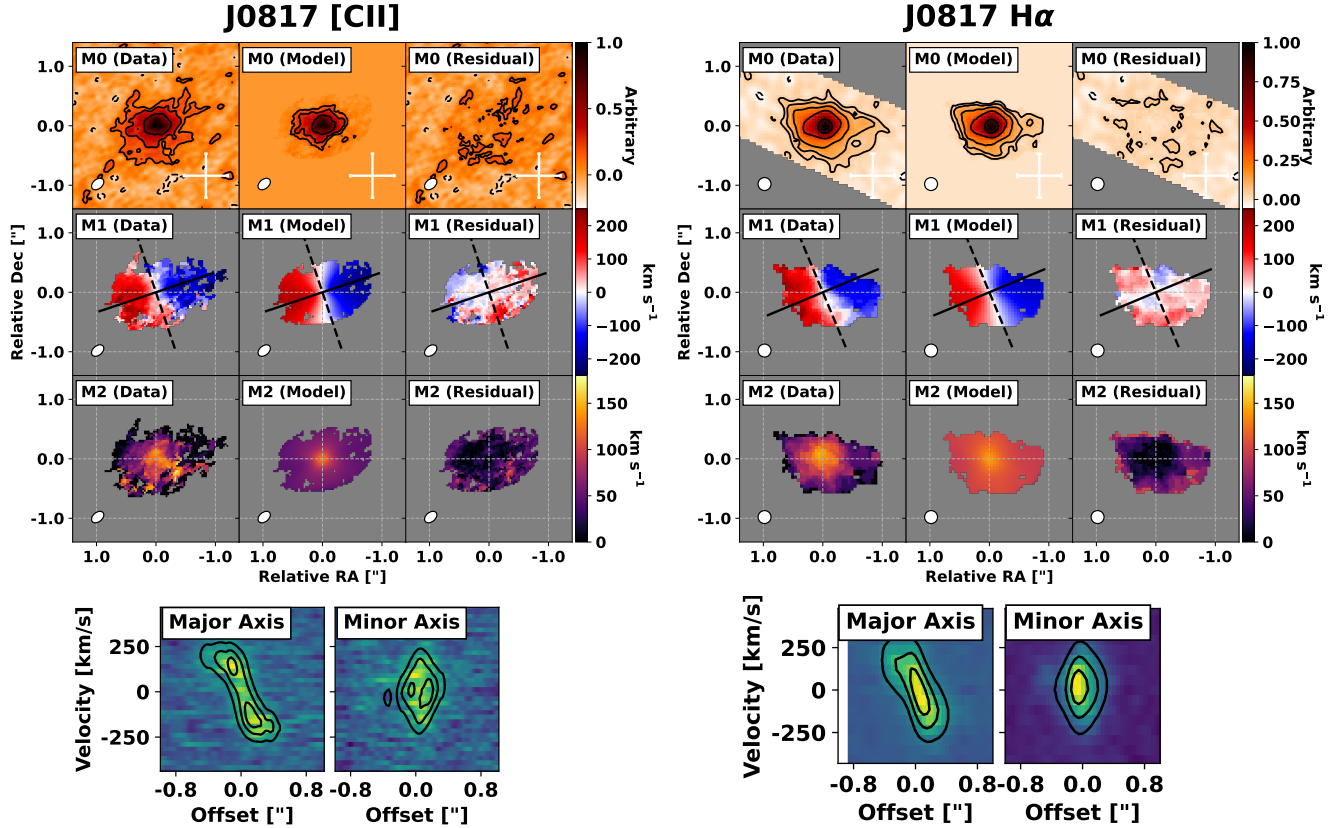


**Figure 6.** Comparison of  $3\text{DBarolo}$  fits to the [C II] (left) and  $\text{H}\alpha$  (right) data cubes. For each, we present the moment 0 (first row), moment 1 (second row), and moment 2 (third row) for the observed data (left column), model (centre column), and the difference between the two (column). The bottom row includes PVDs extracted from the observed data cube (colours) and model (contours) along the major (lower left) and minor (lower right) axes. The white crosses in the top row show a scale of  $5 \text{ kpc} \times 5 \text{ kpc}$ .

while a possible morphological [C II]- $\text{H}\alpha$  offset is visible by eye in Figure 1 and the `PYSERSIC` fits report a small offset, our  $3\text{DBarolo}$  fits lead us to conclude that the kinematic centres of the [C II] and  $\text{H}\alpha$  emission are aligned.

As noted in Section 2.2, the [C II] data for this galaxy have already been analysed by multiple works. This opens a useful avenue to verify our approach through comparisons to previous analyses of the same galaxy that used a variety of dynamical fitting codes, as shown in the right column of Figure 7. The first (Jones et al. 2017; purple dotted line) used the *rotcur* task from the ‘The Groningen Image Processing SYstem’ package (`GIPSY`; van der Hulst et al. 1992) to fit a tilted ring model to the velocity field of the low-resolution [C II] data ( $2015.1.01564.S$ ;  $\sim 0.8''$  resolution; see Section 2.2). The beam size was not included in the modelling, resulting in significant beam smearing, as seen in a steeper profile than later analyses.

On the other hand, Neeleman et al. (2020) and Roman-Oliveira et al. (2023) used the codes `QUBEFIT` and  $3\text{DBarolo}$ , respectively. While both perform a fit to the full data cube (i.e., not only moment maps) and account for the PSF,  $3\text{DBarolo}$  uses a model composed of several rings (see Section 4.1) while `QUBEFIT` is a parametric code and fits for the best parameters of a brightness profile (e.g., exponential disk) and rotation curve (e.g., linear or arctangent, with constant velocity dispersion). The different approaches yield similar rotation curves, but different velocity dispersion profiles. Since we use  $3\text{DBarolo}$  as well, our results are in agreement with those of Roman-Oliveira et al. (2024).

## 5 DISCUSSION

### 5.1 Rotational support throughout cosmic time

When considering the role of kinematics in galaxy evolution, one useful observable is the rotational support (quantified by the ratio of  $v_{\text{rot}}/\sigma_v$ ). While it is common to examine the redshift evolution of this ratio (e.g., Wisnioski et al. 2015; Simons et al. 2016, 2017; Wisnioski et al. 2019; Gillman et al. 2019; Molina et al. 2019a; Danhaive et al. 2025; Pascalau et al. 2025), most comparisons either only consider one phase of the ISM or mix tracers of multiple phases. But as discussed in Section 1, the different phases of the ISM traced by various emission lines result in different measurements of this ratio. Here, we combine the results of our analysis with those from literature to compare this ratio as derived from tracers of ionised gas (i.e.,  $\text{H}\alpha$ , [O III] $\lambda 5007$ , [O III] $88 \mu\text{m}$ ) and molecular gas (i.e., CO, [C II]).

#### 5.1.1 Literature analysis

For the ionised gas (left panel of Figure 8), galaxies at  $z \lesssim 4$  feature a wide range of rotational support, including both highly rotation-dominated with  $(v_{\text{rot}}/\sigma_v)_{\text{ionised}} > 10$  and dispersion-dominated sources with  $(v_{\text{rot}}/\sigma_v)_{\text{ionised}} < 1$ . However, the upper envelope of these values approximately follows the predicted  $(v_{\text{rot}}/\sigma_v)_{\text{ionised}}$  evolution for  $9.0 < \log_{10}(M_*/M_\odot) < 11.0$  star-forming galaxies from Pillepich et al. (2019). A more representative profile is given by

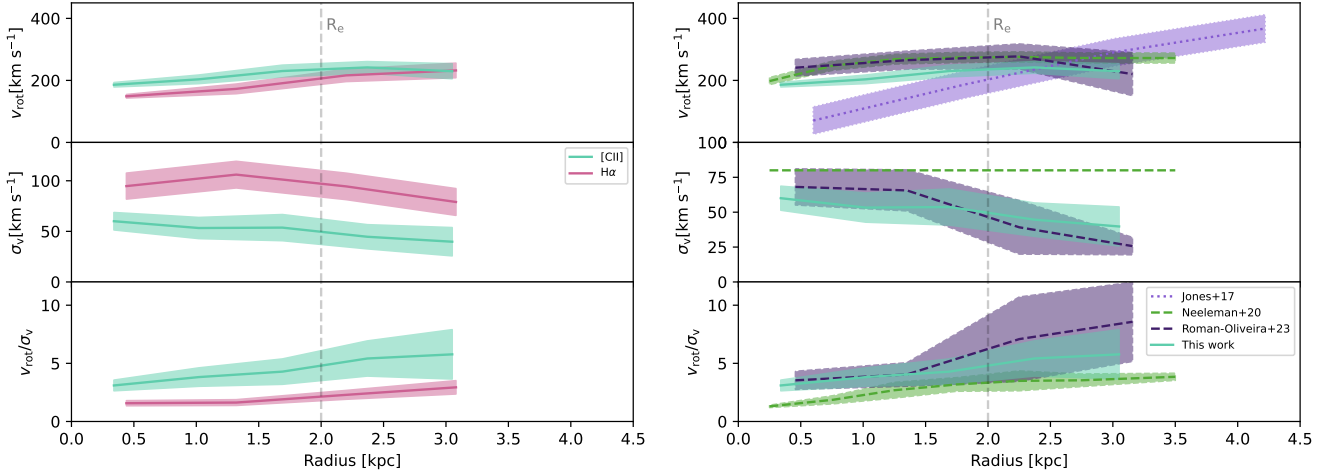


**Figure 7.** Comparison of best-fit rotation curves (top panels), velocity dispersion profiles (centre panels), and the ratio of the two (lower panels) for the [C II] and H $\alpha$  data studied in this work (left column). In the right column, we compare our [C II] values for DLA0817g1 to those of previous works that studies the same galaxy (Jones et al. 2017; Neeleman et al. 2020; Roman-Oliveira et al. 2023). For each panel, we mark the effective radius of the H $\alpha$  emission (as derived through a Sérsic fit; Section 3.1) with a dashed vertical line.

the blue curve, which shows the expected  $(v_{\text{rot}}/\sigma_v)_{\text{H}\alpha}$  evolution of  $M_* = 10^{10.5} M_\odot$  galaxies (Wisnioski et al. 2015), as based on the Toomre stability criterion (Toomre 1964) and the gas fraction evolution (Tacconi et al. 2013; Whitaker et al. 2014). Similarly, galaxies at  $z \gtrsim 4$  feature a large scatter in rotational support, with the most rotation-dominated sources comparable to the expected evolution of H $\alpha$ -traced kinematics from the SERRA simulation (Kohandel et al. 2024)<sup>8</sup>.

For galaxies at  $z \lesssim 5$ , the molecular gas rotational support follows the best-fit relation of Rizzo et al. (2024). Higher-redshift sources are less numerous, but again the most extreme sources lie near the Kohandel et al. (2024) relation for [C II].

Our values for DLA0817g1 lie near the intersection of models in each panel, representing that this source exhibits strong rotational support that is expected from simulations and observations of multiple ISM phases. Notably, DLA0817g1 is not the most extreme  $z \sim 4$  rotator in either phase - exhibiting a lower  $(v_{\text{rot}}/\sigma_v)_{\text{ionised}}$  than AGN host galaxies (Parlanti et al. 2024; Übler et al. 2024) and a lower  $(v_{\text{rot}}/\sigma_v)_{\text{molecular}}$  than dusty SFGs (Roman-Oliveira et al. 2023; Venkateshwaran et al. 2024; Amvrosiadis et al. 2025). Instead, it is more similar to a representative rotator, as evidenced by its similarity to the  $(v_{\text{rot}}/\sigma_v)_{\text{ionised}}$  of the sample of Danhaive et al. (2025) and the  $(v_{\text{rot}}/\sigma_v)_{\text{molecular}}$  of the sample of Jones et al. (2021) - both of which included ‘normal’ (i.e., not starburst, AGN, or quenched) galaxies.

### 5.1.2 Comment on archival sample

There are several caveats of this presentation of the data that are required for proper interpretation. First, the archival sample features large variety in galaxy properties, including stellar mass (e.g., the sample of Danhaive et al. 2025 spans  $8.0 < \log_{10}(M_*/M_\odot) < 10.0$ ), presence of AGN (e.g., Parlanti et al. 2024; Übler et al. 2024), origin of data (e.g.; JWST/NIRCam grism, Danhaive et al. 2025; JWST/NIRSpec MSA, de Graaff et al. 2024; ALMA, Lelli et al.

2021; JWST/NIRSpec IFU, Arribas et al. 2024), and dynamical fitting method (e.g.; DYSMAL, Genzel et al. 2017; Übler et al. 2024; <sup>3D</sup>Barolo, Pope et al. 2023; Posses et al. 2023; GEKO, Danhaive et al. 2025). While a few studies fit the ionised and molecular gas kinematics in a similar fashion for the same sample (e.g., Parlanti et al. 2023), different galaxies are presented in the two panels. These differences allow us to compare a large number of galaxies (e.g., compared to an analysis only using ALMA [C II] data and <sup>3D</sup>Barolo), but is crucial to note that this does not represent a uniform population.

Next, we note that this sample is biased against dispersion-dominated sources due to the fact that some archival studies only studied known rotators or only report  $(v_{\text{rot}}/\sigma_v)$  for rotators (e.g., Jones et al. 2021; Rowland et al. 2024; Übler et al. 2024; Amvrosiadis et al. 2025). While a few studies report this ratio for their full sample (e.g., Turner et al. 2017; Gillman et al. 2019), the values in Figure 8 represent some of the most rotationally-supported galaxies yet observed.

While we restrict our analysis to the redshift range that contains many measurements of molecular gas kinematics ( $z < 8$ ), we note that other works have explored the ionised gas kinematics at higher redshift. These include [O III] $\lambda 5007$  at  $z = 8.34$  (Li et al. 2023), [O III] $88 \mu\text{m}$  at  $z = 9.1$  (Tokuoka et al. 2022), C III] $\lambda\lambda 1907, 1910$  at  $z = 10.6$  (Xu et al. 2024), and [O III] $88 \mu\text{m}$  at  $z = 14.18$  (Scholtz et al. 2025b).

## 5.2 Mass of DLA0817g1

### 5.2.1 Dynamical mass

Our <sup>3D</sup>Barolo analysis allows us to estimate the total dynamical mass of the system. While some works estimate the dynamical mass of a rotating disk galaxy using only the observed rotational velocity ( $M_{\text{dyn}}(r < R_e) = R_e v_{\text{rot}}(R_e)^2/G$ ; e.g., De Breuck et al. 2014; Jones et al. 2017), this approach is only valid for sources with extremely high rotational support (i.e.,  $v_{\text{rot}}/\sigma > 10$ ; Phillips et al. 2025). More generally, the contribution of support from random motion must be taken into account - an effect generally labelled as the asymmetric drift correction. A common approach is to assume that the host galaxy features an exponential brightness profile (equivalent to a

<sup>8</sup> While the  $(v_{\text{rot}}/\sigma_v)$  values of Kohandel et al. (2024) feature significant uncertainties, they are not included here because they are neither reported nor measurable in their figure.

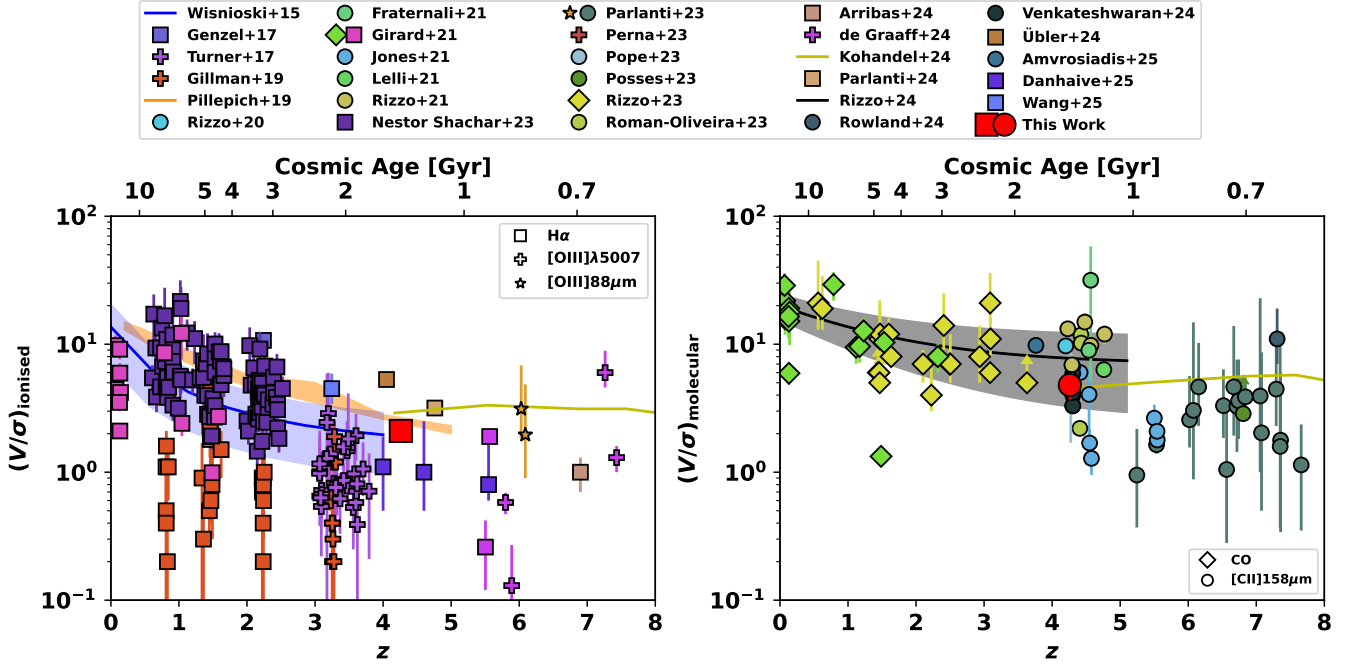


**Figure 8.** Collection of rotational velocity to velocity dispersion ratios, for ionised (left panel) and molecular gas (right panel). In addition to the values of DLA0817g1 (red points), we include values from literature for ionised gas (Genzel et al. 2017; Turner et al. 2017; Gillman et al. 2019; Girard et al. 2021; Nestor Shachar et al. 2023; Perna et al. 2023; Arribas et al. 2024; de Graaff et al. 2024; Parlanti et al. 2024; Übler et al. 2024; Danhaive et al. 2025; Wang et al. 2025) and molecular gas (Rizzo et al. 2020; Fraternali et al. 2021; Lelli et al. 2021; Rizzo et al. 2021; Jones et al. 2021; Parlanti et al. 2023; Pope et al. 2023; Posses et al. 2023; Rizzo et al. 2023; Roman-Oliveira et al. 2023; Rowland et al. 2024; Venkateshwaran et al. 2024; Amvrosiadis et al. 2025). Some studies present results from both gas phases (Girard et al. 2021; Parlanti et al. 2023). The black line in the right panel depicts the best-fit  $(v_{\text{rot}}/\sigma_v)_{\text{molecular}}$  relation from Rizzo et al. (2024), with the reported scatter is depicted as a shaded region. The blue curve in the left panel shows the expected  $(v_{\text{rot}}/\sigma_v)_{\text{H}\alpha}$  evolution of  $M_* = 10^{10.5} M_\odot$  galaxies (Wisnioski et al. 2015). The observed values are compared to expected ratios from simulations: the orange shaded region in the left panel shows the  $\text{H}\alpha$  ratio from TNG50 for  $\log_{10}(M_*/M_\odot) = 9 - 11$  galaxies (Pillepich et al. 2019), while the olive lines at  $z > 4$  in the left and right panels show  $(v_{\text{rot}}/\sigma_v)$  for  $\log_{10}(M_*/M_\odot) = 9 - 10$  galaxies from the SERRA simulations for  $\text{H}\alpha$  and  $[\text{C II}]$ , respectively (Kohandel et al. 2024).

Sérsic index of  $n_s = 1$ ), resulting in a so-called ‘circular velocity’ of  $v_{\text{circ}} = \sqrt{v_{\text{rot}}^2 + 3.36\sigma^2}$  (e.g., Genzel et al. 2017; Förster Schreiber et al. 2018; Price et al. 2020; Danhaive et al. 2025). This circular velocity may be used to estimate the total dynamical mass:

$$M_{\text{dyn}} = k_{\text{tot}} \frac{R_e v_{\text{circ}}(R_e)^2}{G} \quad (6)$$

where the virial coefficient  $k_{\text{tot}}$  is dependent on the geometry of the galaxy (i.e.,  $n_s$  and intrinsic spheroid axis ratio  $q_0 \equiv c/a$ ; e.g., Price et al. 2022).

To apply equation 6 to our data, we use the PYSERVIC fits of the  $\text{H}\alpha$  and  $[\text{C II}]$  data performed in Section 3.1. The results of Price et al. (2022) may then be used to calculate  $k_{\text{tot}} = 2.1 \pm 0.3$  (assuming a nearly flat disk of  $q_0 = 0.4 \pm 0.2$ ).

To allow for easier comparison to previous analyses, we approximate the galaxy as an exponential disk (which is in agreement with our Sérsic fits), enabling the use of the previously defined circular velocity. By interpolating the best-fit rotation curves and velocity dispersion curves (Figure 7), we find a total dynamical mass of  $\log_{10}(M_{\text{dyn}}/M_\odot) \sim 10.9$  for both tracers (Table 5), in agreement with previous results (e.g., Neeleman et al. 2020)<sup>9</sup>.

<sup>9</sup> We do not discuss the  $[\text{C II}]$ -based dynamical mass estimates of Jones et al. (2017) and Jones et al. (2020) due to a lack of PSF treatment and asymmetric drift correction, respectively.

### 5.2.2 Molecular gas mass

Based on CO(2-1) observations, Neeleman et al. (2020) estimate the gas mass of DLA0817g1 to be  $\log_{10}(M_{\text{H}_2}/M_\odot) = 10.9^{+0.1}_{-0.2}$  (assuming  $r_{21} = 0.81$ ,  $\alpha_{\text{CO}} = 3.0 M_\odot \text{ K}^{-1} \text{ km}^{-1} \text{ s pc}^{-2}$ ). However, the necessary factors to convert from  $L_{\text{CO}(2-1)}$  to  $M_{\text{H}_2}$  (i.e.,  $r_{21}$ ,  $\alpha_{\text{CO}}$ ) have been found to vary within galaxies (e.g., Hu et al. 2022; Teng et al. 2022; Anirudh et al. 2025), with  $\alpha_{\text{CO}}$  featuring a strong dependence on metallicity (e.g., Narayanan et al. 2012; Madden et al. 2020). The fact that this mass is comparable to the dynamical mass introduces some doubt as to the applicability of the conversion factors.

While the factor  $r_{21}$  has been observed to feature a significant variation within a galaxy (e.g., Yajima et al. 2021; Leroy et al. 2022), the spatially integrated factors usually only vary by a factor of  $\lesssim 2$  (e.g., Carilli & Walter 2013; Maeda et al. 2022). Increasing  $r_{21}$  from 0.81 (as assumed by Neeleman et al. 2020) to an extreme value of unity (appropriate for quasar host galaxies; Carilli & Walter 2013) results in a  $< 1\sigma$  decrease in  $M_{\text{mol}}$ , so the assumed  $r_{21}$  value is likely not the source of this high gas mass.

A number of metallicity-dependent formulations of  $\alpha_{\text{CO}}$  have been measured (e.g., Glover & Mac Low 2011; Schrubba et al. 2012; Bolatto et al. 2013; Genzel et al. 2015; Amorín et al. 2016; Accurso et al. 2017; Tacconi et al. 2018, as collected by Madden et al. 2020), which yield a large range of  $\alpha_{\text{CO}} \sim 3 - 20 M_\odot \text{ K}^{-1} \text{ km}^{-1} \text{ s pc}^{-2}$  for  $Z/Z_\odot \sim 0.7$ . Since a higher  $\alpha_{\text{CO}}$  for a given  $L'_{\text{CO}}$  will result in a higher estimated gas mass, these values would only result in an estimated



gas mass greater than the dynamical mass. On the other hand, the Narayanan et al. (2012) calibration (which includes a dependence on the integrated CO luminosity) yields  $\alpha_{\text{CO}} \sim 0.5 M_{\odot} \text{ K}^{-1} \text{ km}^{-1} \text{ s pc}^{-2}$  and  $M_{\text{H}_2} \sim 10^{10.0} M_{\odot}$ . So while a high  $\alpha_{\text{CO}}$  may be the culprit behind the large gas mass estimate, further analysis of this conversion factor at high redshift is needed.

While [C II] line has historically been used a tracer of SFR (e.g., De Looze et al. 2014; Schaerer et al. 2020) and  $M_{\text{HI}}$  (e.g., Heintz et al. 2021), it has seen great recent success as a tracer of  $M_{\text{H}_2}$  (e.g., Zanella et al. 2018; Dessauges-Zavadsky et al. 2020; Vizgan et al. 2022). To update this estimate of  $M_{\text{H}_2}$ , we adopt the metallicity-dependent  $L_{[\text{CII}]}-M_{\text{H}_2}$  conversion of Vallini et al. (2025). Using the gas-phase metallicity derived from our data (Table 3) results in  $\alpha_{[\text{CII}]} \equiv M_{\text{gas}}/L_{[\text{CII}]} = 5.4 M_{\odot}/L_{\odot}$ , and  $\log_{10}(M_{\text{gas},[\text{CII}]} / M_{\odot}) = 10.24 \pm 0.05$  (see Table 3; assuming the  $L_{[\text{CII}]}$  value of Neeleman et al. 2020). This is  $\sim 0.6$  dex lower than the previously determined  $M_{\text{H}_2,\text{CO}}$  and  $M_{\text{dyn}}$ , leaving space in the mass budget for a stellar component.

We note that the previous work of Zanella et al. (2018) found a much higher  $\alpha_{[\text{CII}]} \sim 30 M_{\odot}/L_{\odot}$ , which would result in a  $\sim 0.8$  dex higher gas mass estimate. However, Rizzo et al. (2021) found that for a sample of  $4 \lesssim z \lesssim 5$  dusty, rotating SFGs (i.e., similar galaxies to DLA0817g1), a lower conversion factor of  $\alpha_{[\text{CII}]} \sim 5 - 20 M_{\odot}/L_{\odot}$  was preferred. Simulations have also found a lower value, in agreement with our estimate (e.g., Gurman et al. 2024; Casavecchia et al. 2025).

### 5.2.3 Other mass components

With the dynamical and molecular gas masses in hand, we may explore constraints on other mass components. As explored in Appendix D, dust likely makes up a small fraction of the mass budget ( $\log_{10}(M_{\text{dust}}/M_{\odot}) \sim 8$ ). By subtracting the [C II]-based molecular gas mass and dust mass from the dynamical mass, we find a remaining mass of  $10^{10.8} M_{\odot}$ . Here, we explore possible contributions to this remaining mass from a stellar component or dark matter halo.

From a dynamical analysis, Roman-Oliveira et al. (2024) estimated a stellar mass for DLA0817g1 of  $\log_{10}(M_{*}/M_{\odot}) = 10.6 \pm 0.2$ , which is in agreement with our remaining mass. If we combine the FIR-based SFR ( $SFR_{160\mu\text{m}} = 118 \pm 14 M_{\odot} \text{ yr}^{-1}$ ; Neeleman et al. 2020) with our dust corrected H $\alpha$ -based SFR ( $SFR_{\text{H}\alpha} = 46 \pm 3 M_{\odot} \text{ yr}^{-1}$ ; Table 3), then this stellar mass would also place DLA0817g1 on the star forming main sequence (adopting the form of Speagle et al. 2014).

On the other hand, the remaining mass may feature a contribution from a dark matter halo. We consider a dark matter halo whose mass density follows an NFW profile (Navarro et al. 1997). The mass within a given radius takes the form (e.g., de Blok et al. 2008):

$$M_{\text{NFW}}(< R) = 4\pi\rho_{\text{crit}}\delta_c \int_0^R \frac{r^2}{(1+r/R_S)^2(r/R_S)} \delta r \quad (7)$$

where  $\rho_{\text{crit}} = 3H^2/8\pi G$  is the critical density of the Universe at a given redshift,  $R_S$  is the characteristic radius of the halo, and  $\delta_c$  is a function of the concentration  $c_{200} \equiv R_{200}/R_S$  (Ludlow et al. 2013). Following other works (e.g., Mitsuhashi et al. 2021; Fraternali et al. 2021; Roman-Oliveira et al. 2024; Neeleman et al. 2025), we adopt  $c_{200} = 3.4$  (valid for halos of mass  $\sim 10^{10.0-12.5} M_{\odot}$  at  $z \sim 4$ ; Dutton & Macciò 2014) and  $R_{200} = 100 \text{ kpc}$  (valid for a halo of mass  $\sim 10^{12} M_{\odot}$ ). This results in an enclosed mass of  $M_{\text{halo}}(r < 3.5 \text{ kpc}) \sim 10^{10.7} M_{\odot}$ . We note that this value is highly dependent on the assumed scale radius, with  $R_{200} = 70 \text{ kpc}$  yielding an enclosed mass that is lower by 0.2 dex.

While a precise estimate of  $M_{*}$  will be determined through HST/JWST/NIRCam spectral energy distribution (SED) fitting in a future work, we note that the current work supports the existence of a substantial stellar component, with a possible contribution from a dark matter halo.

### 5.3 Nature of DLA0817g1

By combining the results of this work with those of previous analyses, we may consider a more complete picture of DLA0817g1. The remarkable agreement of the [C II] and H $\alpha$  morpho-kinematics confirms that this is a relaxed rotating disk, with no significant evidence for ongoing major mergers, outflows, or AGN (from the WHAN diagram). It is [C II]-luminous, with a FIR-based SFR that far exceeds the NUV- or H $\alpha$ -based values - suggesting a high fraction of obscured star formation. This is further supported by a preliminary FIR SED analysis, which shows evidence for a significant dust reservoir. We also find a relatively high gas-phase metallicity ( $0.7 \pm 0.1$  solar), implying a history of chemical enrichment.

It is clear that this source is not undergoing a major starburst episode, as evidenced by the low ionization parameter and our electron temperature (although the latter requires additional emission line detections to be confirmed). Its electron density and degree of rotational support (as traced by emission lines from the ionised and molecular ISM) are similar to ‘normal’ (i.e., representative of the most numerous population of observed sources) galaxies at  $z \sim 4$ . Our estimates of the molecular gas mass show that this is not a gas-dominated source ( $f_{\text{gas}} \sim 1$ ), as previously suggested, but instead contains a large gas reservoir, with room in the mass budget for a significant stellar population and a dark matter halo.

From this, we label DLA0817g1 as a ‘smouldering’ disk galaxy - one that has a history of significant star formation (resulting in a high metallicity and a dust reservoir that obscures ongoing star formation), but is not currently highly excited (based on the low  $U$  and  $T_e$ ). This maturity is noteworthy, as its high redshift means that it only had  $\lesssim 1.4$  Gyr to evolve. Our dynamical analysis implies that the material in this galaxy has relaxed into a disc, with any signatures of major disturbances already faded. Further properties (e.g., stellar mass, star formation history, possible stellar rotation) are deferred to future analyses

## 6 CONCLUSIONS

In this work, we present new high spectral resolution ( $R \sim 2700$ ) JWST/NIRSpec IFU observations of the rotating disk galaxy DLA0817g1. Combining our data with archival ALMA observations allows us to explore the multi-phase morphology, kinematics, and ISM conditions of this  $z \sim 4$  galaxy.

By combining the fluxes of our detected emission lines with the upper limits of undetected lines and the code PYNEB, we find evidence for a low electron temperature ( $T_e = (1.2^{+0.7}_{-0.5}) \times 10^4 \text{ K}$ ), no strong evidence for significant dust attenuation ( $E(B-V) = 0.4^{+0.5}_{-0.3}$ ), and a electron density that is in agreement with the redshift-dependent correlation of previous works ( $\log_{10}(n_e[\text{cm}^{-3}]) = 2.5 \pm 0.4$ ). A strong-line metallicity calibration yields a high metallicity for this redshift ( $0.7 \pm 0.1$  solar), while the S32 ratio is used to predict a relatively low ionization parameter ( $\log_{10}(U) \sim -3.5$ ). Despite only having one observed Balmer transition, we use the WHAN diagnostic to show that a lack of evidence for the presence of an AGN (but note that this is not the same as evidence for the lack of an AGN).

The [C II] and H $\alpha$  emission show remarkably similar morphokinematics. Sérsic profile fits to the integrated maps of each result in best-fit parameters that are in agreement, while both lines show similar line of sight velocity (moment 1) and velocity dispersion (moment 2) maps. Through <sup>3D</sup>Barolo fits to each data cube, we demonstrate that while the two tracers exhibit the same rotational velocity, H $\alpha$  features a velocity dispersion that is  $\sim 2\times$  that of [C II].

We then consider the redshift evolution of rotational support (quantified by  $v_{\text{rot}}/\sigma_v$ ) in the ionised and molecular phases of the ISM. In addition to the results of the <sup>3D</sup>Barolo fit of DLA0817g1, we compile a large comparison sample of archival values from observations and simulations. This shows that not only does the higher  $(v_{\text{rot}}/\sigma_v)_{\text{[CII]}}$  agree with previous findings for  $z \sim 4$  galaxies (suggesting that H $\alpha$  traces extraplanar gas in addition to the disk), but the observed ratios for DLA0817g1 are in agreement with the theoretical and simulated ratios of disk galaxies - making DLA0817g1 a prime laboratory for studying disks in the early Universe.

We combine our new estimate of the gas-phase metallicity with metallicity-dependent conversion factors to estimate the molecular gas mass of DLA0817g1 using the CO(2-1) and [C II] luminosities. With these factors, we no longer find the previously reported extreme  $M_{\text{H}_2}$  (which was comparable to the dynamical mass), but instead a gas mass that is  $\sim 20\%$  of the dynamical mass. This leaves space in the mass budget for a sizeable stellar mass (as suggested by previous mass decomposition analyses) or a dark matter halo.

Finally, we synthesise our findings to explore the nature of DLA0817g1, finding that it is a representative galaxy (in terms of rotational support, electron density, and possibly starburstiness) undergoing ordered rotation (as traced by the molecular and ionised gas), with signs of past star formation (i.e., high  $Z$ , evidence for dust, low  $U$ ) and potential for more SF (sizeable molecular gas reservoir). Future works will explore additional properties (e.g., the stellar mass, the presence of AGN or a Ly $\alpha$  halo).

## ACKNOWLEDGEMENTS

GCJ, FDE, and JS acknowledge support by the Science and Technology Facilities Council (STFC), by the ERC through Advanced Grant 695671 “QUENCH”, and by the UKRI Frontier Research grant RISEandFALL. SA, MP, and BRP acknowledge support from the research projects PID2021-127718NB-I00, PID2024-159902NA-I00, PID2024-158856NA-I00, and RYC2023-044853-I of the Spanish Ministry of Science and Innovation/State Agency of Research (MCIN/AEI/10.13039/501100011033), FSE+, and by “ERDF A way of making Europe”. AJB acknowledges funding from the “First-Galaxies” Advanced Grant from the European Research Council (ERC) under the European Union’s Horizon 2020 research and innovation programme (Grant agreement No. 789056). GC acknowledges the support of the INAF Large Grant 2022 “The metal circle: a new sharp view of the baryon cycle up to Cosmic Dawn with the latest generation IFU facilities” and the INAF GO grant “A JWST/MIRI MIRACLE: Mid-IR Activity of Circumnuclear Line Emission”. IL acknowledges support from PRIN-MUR project “PROMETEUS” financed by the European Union - Next Generation EU, Mission 4 Component 1 CUP B53D23004750006. HÜ acknowledges funding by the European Union (ERC APEX, 101164796). Views and opinions expressed are however those of the authors only and do not necessarily reflect those of the European Union or the European Research Council Executive Agency. Neither the European Union nor the granting authority can be held responsible for them. SZ acknowledges support from the European Union (ERC, WINGS,

101040227). This paper makes use of the following ALMA data: ADS/JAO.ALMA#2017.1.01052. ALMA is a partnership of ESO (representing its member states), NSF (USA) and NINS (Japan), together with NRC (Canada), MOST and ASIAA (Taiwan), and KASI (Republic of Korea), in cooperation with the Republic of Chile. The Joint ALMA Observatory is operated by ESO, AUI/NRAO and NAOJ.

## DATA AVAILABILITY

The JWST/NIRSpec IFU data studied here (Project 4528, observation 7) will be publically available from the MAST archive on 8 December, 2025. The ALMA data studied in this work is available from the ALMA archive (<https://almascience.eso.org/aq/>) under project code 2017.1.01052.

## REFERENCES

- Accurso G., et al., 2017, *MNRAS*, **470**, 4750
- Allende Prieto C., Lambert D. L., Asplund M., 2001, *ApJ*, **556**, L63
- Amorín R., Muñoz-Tuñón C., Aguerrí J. A. L., Planesas P., 2016, *A&A*, **588**, A23
- Amvrosiadis A., et al., 2025, *MNRAS*, **537**, 1163
- Anirudh R., Kaasinen M., Popping G., Narayanan D., García K., Valentín-Martínez D., 2025, *A&A*, **699**, A19
- Arribas S., et al., 2024, *A&A*, **688**, A146
- Assef R. J., et al., 2016, *ApJ*, **819**, 111
- Baldwin J. A., Phillips M. M., Terlevich R., 1981, *PASP*, **93**, 5
- Begeman K. G., Broeils A. H., Sanders R. H., 1991, *MNRAS*, **249**, 523
- Béthermin M., Doré O., Lagache G., 2012, *A&A*, **537**, L5
- Bianchin M., et al., 2024, *ApJ*, **965**, 103
- Böker T., et al., 2022, *A&A*, **661**, A82
- Bolatto A. D., Wolfire M., Leroy A. K., 2013, *ARA&A*, **51**, 207
- Bouwens R. J., et al., 2022, *ApJ*, **931**, 160
- Buchner J., 2021, *The Journal of Open Source Software*, **6**, 3001
- Burbidge E. M., Burbidge G. R., 1959, *ApJ*, **129**, 271
- Burbidge E. M., Burbidge G. R., Prendergast K. H., 1960, *ApJ*, **132**, 640
- Bushouse H., et al., 2024, JWST Calibration Pipeline, doi:10.5281/zenodo.12692459
- CASA Team et al., 2022, *PASP*, **134**, 114501
- Calzetti D., Armus L., Bohlin R. C., Kinney A. L., Koornneef J., Storchi-Bergmann T., 2000, *ApJ*, **533**, 682
- Caputi K. I., et al., 2017, *ApJ*, **849**, 45
- Carilli C. L., Walter F., 2013, *ARA&A*, **51**, 105
- Carniani S., et al., 2013, *A&A*, **559**, A29
- Casavecchia B., Maio U., Péroux C., Ciardi B., 2025, *A&A*, **693**, A119
- Casertano S., 1983, *MNRAS*, **203**, 735
- Ceci M., et al., 2025, *A&A*, **695**, A116
- Chabrier G., 2003, *PASP*, **115**, 763
- Choustikov N., et al., 2025, *arXiv e-prints*, p. arXiv:2510.06347
- Cid Fernandes R., Stasińska G., Schlickmann M. S., Mateus A., Vale Asari N., Schoenell W., Sodr   L., 2010, *MNRAS*, **403**, 1036
- Cid Fernandes R., Stasińska G., Mateus A., Vale Asari N., 2011, *MNRAS*, **413**, 1687
- Cortese L., Catinella B., Janowiecki S., 2017, *ApJ*, **848**, L7
- Curti M., Mannucci F., Cresci G., Maiolino R., 2020, *MNRAS*, **491**, 944
- Curti M., et al., 2024, *A&A*, **684**, A75
- D’Eugenio F., et al., 2024, *Nature Astronomy*, **8**, 1443
- D’Eugenio F., et al., 2025, *MNRAS*, **536**, 51
- Danhaive A. L., et al., 2025, *arXiv e-prints*, p. arXiv:2503.21863
- Davis T. A., et al., 2013, *MNRAS*, **429**, 534
- De Breuck C., et al., 2014, *A&A*, **565**, A59
- De Looze I., et al., 2014, *A&A*, **568**, A62
- Dessauges-Zavadsky M., et al., 2020, *A&A*, **643**, A5
- Di Teodoro E. M., Fraternali F., 2015, *MNRAS*, **451**, 3021

- Driver S. P., Robotham A. S. G., Bland-Hawthorn J., Brown M., Hopkins A., Liske J., Philipps S., Wilkins S., 2013, *MNRAS*, **430**, 2622
- Dutton A. A., Macciò A. V., 2014, *MNRAS*, **441**, 3359
- Dutton A. A., van den Bosch F. C., Dekel A., 2010, *MNRAS*, **405**, 1690
- Fan L., Knudsen K. K., Han Y., Tan Q.-h., 2019, *ApJ*, **887**, 74
- Figueira M., et al., 2022, *A&A*, **667**, A29
- Förster Schreiber N. M., et al., 2009, *ApJ*, **706**, 1364
- Förster Schreiber N. M., et al., 2018, *ApJS*, **238**, 21
- Fraternali F., Karim A., Magnelli B., Gómez-Guijarro C., Jiménez-Andrade E. F., Posses A. C., 2021, *A&A*, **647**, A194
- Fruchter A. S., Hook R. N., 2002, *PASP*, **114**, 144
- Fujimoto S., et al., 2025, *Nature Astronomy*, **9**, 1553
- Gaia Collaboration et al., 2016, *A&A*, **595**, A1
- Gaia Collaboration et al., 2021, *A&A*, **649**, A1
- Genzel R., et al., 2013, *ApJ*, **773**, 68
- Genzel R., et al., 2015, *ApJ*, **800**, 20
- Genzel R., et al., 2017, *Nature*, **543**, 397
- Gillman S., et al., 2019, *MNRAS*, **486**, 175
- Girard M., et al., 2021, *ApJ*, **909**, 12
- Glover S. C. O., Mac Low M.-M., 2011, *MNRAS*, **412**, 337
- González V., Labbé I., Bouwens R. J., Illingworth G., Franx M., Kriek M., Brammer G. B., 2010, *ApJ*, **713**, 115
- Gurman A., Hu C.-Y., Sternberg A., van Dishoeck E. F., 2024, *ApJ*, **965**, 179
- Gururajan G., et al., 2022, *A&A*, **663**, A22
- Harikane Y., et al., 2020, *ApJ*, **896**, 93
- Heintz K. E., Watson D., Oesch P. A., Narayanan D., Madden S. C., 2021, *ApJ*, **922**, 147
- Herrera-Camus R., et al., 2025, *A&A*, **699**, A80
- Hodge J. A., Carilli C. L., Walter F., de Blok W. J. G., Riechers D., Daddi E., Lentati L., 2012, *ApJ*, **760**, 11
- Hsiao T. Y.-Y., et al., 2024a, *ApJ*, **973**, 8
- Hsiao T. Y.-Y., et al., 2024b, *ApJ*, **973**, 81
- Hu C.-Y., Schruha A., Sternberg A., van Dishoeck E. F., 2022, *ApJ*, **931**, 28
- Isobe Y., Ouchi M., Nakajima K., Harikane Y., Ono Y., Xu Y., Zhang Y., Umeda H., 2023, *ApJ*, **956**, 139
- Jakobsen P., et al., 2022, *A&A*, **661**, A80
- Jones G. T., Stanway E. R., 2023, *MNRAS*, **525**, 5720
- Jones G. C., et al., 2017, *ApJ*, **850**, 180
- Jones G. C., Maiolino R., Caselli P., Carniani S., 2020, *MNRAS*, **498**, 4109
- Jones G. C., et al., 2021, *MNRAS*, **507**, 3540
- Jones G. C., et al., 2024, *arXiv e-prints*, p. [arXiv:2412.15027](https://arxiv.org/abs/2412.15027)
- Jones G. C., et al., 2025a, *arXiv e-prints*, p. [arXiv:2509.20455](https://arxiv.org/abs/2509.20455)
- Jones G. C., et al., 2025b, *MNRAS*, **540**, 3311
- Kennicutt Robert C. J., 1998, *ApJ*, **498**, 541
- Kerrison E. F., Allison J. R., Moss V. A., Sadler E. M., Rees G. A., 2024, *MNRAS*, **533**, 4248
- Kewley L. J., Heisler C. A., Dopita M. A., Lumsden S., 2001, *ApJS*, **132**, 37
- Kewley L. J., Nicholls D. C., Sutherland R. S., 2019, *ARA&A*, **57**, 511
- Kiyota T., et al., 2025, *arXiv e-prints*, p. [arXiv:2504.03156](https://arxiv.org/abs/2504.03156)
- Kohandel M., Pallottini A., Ferrara A., Zanella A., Rizzo F., Carniani S., 2024, *A&A*, **685**, A72
- Lai T. S. Y., et al., 2023, *ApJ*, **957**, L26
- Le Fèvre O., et al., 2020, *A&A*, **643**, A1
- Lelli F., Di Teodoro E. M., Fraternali F., Man A. W. S., Zhang Z.-Y., De Breuck C., Davis T. A., Maiolino R., 2021, *Science*, **371**, 713
- Leroy A. K., et al., 2022, *ApJ*, **927**, 149
- Levy R. C., et al., 2018, *ApJ*, **860**, 92
- Li Z., et al., 2023, *arXiv e-prints*, p. [arXiv:2310.09327](https://arxiv.org/abs/2310.09327)
- Li S., et al., 2025a, *ApJ*, **979**, L13
- Li S., et al., 2025b, *ApJ*, **993**, L51
- Lindblad B., 1927, *MNRAS*, **87**, 553
- Longhetti M., Saracco P., 2009, *MNRAS*, **394**, 774
- Ludlow A. D., et al., 2013, *MNRAS*, **432**, 1103
- Luridiana V., Morisset C., Shaw R. A., 2015, *A&A*, **573**, A42
- Madau P., Dickinson M., 2014, *ARA&A*, **52**, 415
- Madden S. C., et al., 2020, *A&A*, **643**, A141
- Maeda F., Egusa F., Ohta K., Fujimoto Y., Habe A., Asada Y., 2022, *ApJ*, **926**, 96
- Mahieu S., et al., 2012, *IEEE Transactions on Terahertz Science and Technology*, **2**, 29
- Maiolino R., et al., 2008, *A&A*, **488**, 463
- Maiolino R., et al., 2024, *A&A*, **687**, A67
- Mancera Piña P. E., et al., 2020, *MNRAS*, **495**, 3636
- Mannucci F., et al., 2009, *MNRAS*, **398**, 1915
- Marconcini C., et al., 2024, *MNRAS*, **533**, 2488
- Mayall N. U., Aller L. H., 1942, *ApJ*, **95**, 5
- Mazzolari G., et al., 2024, *A&A*, **691**, A345
- Mitsuhashi I., et al., 2021, *ApJ*, **907**, 122
- Molina J., et al., 2019a, *MNRAS*, **482**, 1499
- Molina J., Ibar E., Smail I., Swinbank A. M., Villard E., Escala A., Sobral D., Hughes T. M., 2019b, *MNRAS*, **487**, 4856
- Narayanan D., Krumholz M. R., Ostriker E. C., Hernquist L., 2012, *MNRAS*, **421**, 3127
- Navarro-Carrera R., Caputi K. I., Iani E., Rinaldi P., Kokorev V., Kerutt J., 2025, *ApJ*, **993**, 194
- Navarro J. F., Frenk C. S., White S. D. M., 1997, *ApJ*, **490**, 493
- Neeleman M., Kanekar N., Prochaska J. X., Rafelski M., Carilli C. L., Wolfe A. M., 2017, *Science*, **355**, 1285
- Neeleman M., Prochaska J. X., Kanekar N., Rafelski M., 2020, *Nature*, **581**, 269
- Neeleman M., Kanekar N., Prochaska J. X., Rafelski M. A., Kahinga L. A., 2025, *ApJ*, **983**, 26
- Nestor Shachar A., et al., 2023, *ApJ*, **944**, 78
- Newville M., Stensitzki T., Allen D. B., Ingargiola A., 2014, LMFIT: Non-Linear Least-Square Minimization and Curve-Fitting for Python, [doi:10.5281/zenodo.11813](https://doi.org/10.5281/zenodo.11813)
- Oort J. H., 1927, *Bull. Astron. Inst. Netherlands*, **3**, 275
- Panther B., Jimenez R., Heavens A. F., Charlot S., 2007, *MNRAS*, **378**, 1550
- Parlanti E., Carniani S., Pallottini A., Cignoni M., Cresci G., Kohandel M., Mannucci F., Marconi A., 2023, *A&A*, **673**, A153
- Parlanti E., et al., 2024, *A&A*, **684**, A24
- Parlanti E., et al., 2025, *A&A*, **695**, A6
- Pascalau R. G., et al., 2025, *arXiv e-prints*, p. [arXiv:2505.06349](https://arxiv.org/abs/2505.06349)
- Pasha I., Miller T. B., 2023, *The Journal of Open Source Software*, **8**, 5703
- Pease F. G., 1918, *Proceedings of the National Academy of Science*, **4**, 21
- Perna M., et al., 2023, *A&A*, **679**, A89
- Perna M., et al., 2024, *A&A*, **690**, A171
- Phillips S., Rizzo F., Kohandel M., Smit R., Pallottini A., 2025, *MNRAS*, **540**, 3196
- Pillepich A., et al., 2019, *MNRAS*, **490**, 3196
- Pineda J. L., Langer W. D., Velusamy T., Goldsmith P. F., 2013, *A&A*, **554**, A103
- Pope A., et al., 2023, *ApJ*, **951**, L46
- Posses A. C., et al., 2023, *A&A*, **669**, A46
- Price S. H., et al., 2020, *ApJ*, **894**, 91
- Price S. H., et al., 2022, *A&A*, **665**, A159
- Rafelski M., Wolfe A. M., Prochaska J. X., Neeleman M., Mendez A. J., 2012, *ApJ*, **755**, 89
- Ramos Padilla A. F., Wang L., van der Tak F. F. S., Trager S. C., 2023, *A&A*, **679**, A131
- Rauscher B. J., et al., 2017, *PASP*, **129**, 105003
- Reddy N. A., et al., 2018, *ApJ*, **869**, 92
- Reddy N. A., et al., 2022, *ApJ*, **926**, 31
- Reddy N. A., Topping M. W., Sanders R. L., Shapley A. E., Brammer G., 2023, *ApJ*, **952**, 167
- Rigby J., et al., 2023, *PASP*, **135**, 048001
- Rizzo F., Vegetti S., Powell D., Fraternali F., McKean J. P., Stacey H. R., White S. D. M., 2020, *Nature*, **584**, 201
- Rizzo F., Vegetti S., Fraternali F., Stacey H. R., Powell D., 2021, *MNRAS*, **507**, 3952
- Rizzo F., et al., 2023, *A&A*, **679**, A129
- Rizzo F., et al., 2024, *A&A*, **689**, A273
- Roman-Oliveira F., Fraternali F., Rizzo F., 2023, *MNRAS*, **521**, 1045
- Roman-Oliveira F., Rizzo F., Fraternali F., 2024, *A&A*, **687**, A35
- Rowland L. E., et al., 2024, *MNRAS*, **535**, 2068
- Rubin V. C., Ford Jr. W. K., Thonnard N., 1980, *ApJ*, **238**, 471
- Salak D., Nakai N., Sorai K., Miyamoto Y., 2020, *ApJ*, **901**, 151



Salpeter E. E., 1955, *ApJ*, **121**, 161

Sánchez S. F., Muñoz-Tuñón C., Sánchez Almeida J., González-Martín O., Pérez E., 2025, *arXiv e-prints*, p. [arXiv:2510.07256](https://arxiv.org/abs/2510.07256)

Sanders R. L., et al., 2025, *arXiv e-prints*, p. [arXiv:2508.10099](https://arxiv.org/abs/2508.10099)

Saxena A., et al., 2023, *A&A*, **678**, A68

Schaerer D., et al., 2020, *A&A*, **643**, A3

Schimek A., et al., 2024, *A&A*, **682**, A98

Scholtz J., et al., 2024, *A&A*, **687**, A283

Scholtz J., et al., 2025a, *MNRAS*,

Scholtz J., et al., 2025b, *MNRAS*,

Schruba A., et al., 2012, *AJ*, **143**, 138

Shao Y., et al., 2017, *ApJ*, **845**, 138

Shapley A. E., et al., 2025, *ApJ*, **980**, 242

Shelest A., Lelli F., 2020, *A&A*, **641**, A31

Simons R. C., et al., 2016, *ApJ*, **830**, 14

Simons R. C., et al., 2017, *ApJ*, **843**, 46

Slipher V. M., 1914, *Popular Astronomy*, **22**, 19

Smit R., et al., 2018, *Nature*, **553**, 178

Sofue Y., Rubin V., 2001, *ARA&A*, **39**, 137

Sommovigo L., et al., 2022, *MNRAS*, **513**, 3122

Speagle J. S., Steinhardt C. L., Capak P. L., Silverman J. D., 2014, *ApJS*, **214**, 15

Stott J. P., et al., 2016, *MNRAS*, **457**, 1888

Tacconi L. J., et al., 2013, *ApJ*, **768**, 74

Tacconi L. J., et al., 2018, *ApJ*, **853**, 179

Takase B., 1967, *PASJ*, **19**, 427

Talia M., et al., 2018, *MNRAS*, **476**, 3956

Taylor M. A., et al., 2025, *ApJ*, **991**, L24

Teng Y.-H., et al., 2022, *ApJ*, **925**, 72

Tiley A. L., et al., 2016, *MNRAS*, **460**, 103

Tokuoka T., et al., 2022, *ApJ*, **933**, L19

Toomre A., 1964, *ApJ*, **139**, 1217

Turner O. J., et al., 2017, *MNRAS*, **471**, 1280

Übler H., et al., 2018, *ApJ*, **854**, L24

Übler H., et al., 2019, *ApJ*, **880**, 48

Übler H., et al., 2024, *MNRAS*, **533**, 4287

Ulvén L., et al., 2025, *A&A*, **693**, A36

Vallini L., et al., 2025, *A&A*, **700**, A117

Veilleux S., Osterbrock D. E., 1987, *ApJS*, **63**, 295

Venkateshwaran A., et al., 2024, *ApJ*, **977**, 161

Vizgan D., et al., 2022, *ApJ*, **929**, 92

Wang W., et al., 2025, *Nature Astronomy*, **9**, 710

Whitaker K. E., et al., 2014, *ApJ*, **795**, 104

Whitler L., Stark D. P., Mason C. A., Tang M., Chen Z., Lu T.-Y., Prieto-Lyon G., Hutter A., 2025, *arXiv e-prints*, p. [arXiv:2510.12019](https://arxiv.org/abs/2510.12019)

Wisnioski E., et al., 2015, *ApJ*, **799**, 209

Wisnioski E., et al., 2019, *ApJ*, **886**, 124

Witstok J., Jones G. C., Maiolino R., Smit R., Schneider R., 2023, *MNRAS*, **523**, 3119

Wolfire M. G., McKee C. F., Hollenbach D., Tielens A. G. G. M., 2003, *ApJ*, **587**, 278

Wuyts S., et al., 2016, *ApJ*, **831**, 149

Xu Y., et al., 2024, *ApJ*, **976**, 142

Yajima Y., et al., 2021, *PASJ*, **73**, 257

Zamora S., et al., 2025, *A&A*, **702**, A102

Zanella A., et al., 2018, *MNRAS*, **481**, 1976

de Blok W. J. G., Walter F., Brinks E., Trachternach C., Oh S.-H., Kennicutt Jr. R. C., 2008, *AJ*, **136**, 2648

de Graaff A., et al., 2024, *A&A*, **684**, A87

de Vaucouleurs G., 1961, *ApJ*, **133**, 405

de Vaucouleurs G., de Vaucouleurs A., 1962, *AJ*, **67**, 113

van Albada T. S., Bahcall J. N., Begeman K., Sancisi R., 1985, *ApJ*, **295**, 305

van der Hulst J. M., Terlouw J. P., Begeman K. G., Zwitter W., Roelfsema P. R., 1992, in Worrall D. M., Biemesderfer C., Barnes J., eds, *Astronomical Society of the Pacific Conference Series Vol. 25, Astronomical Data Analysis Software and Systems I*. p. 131

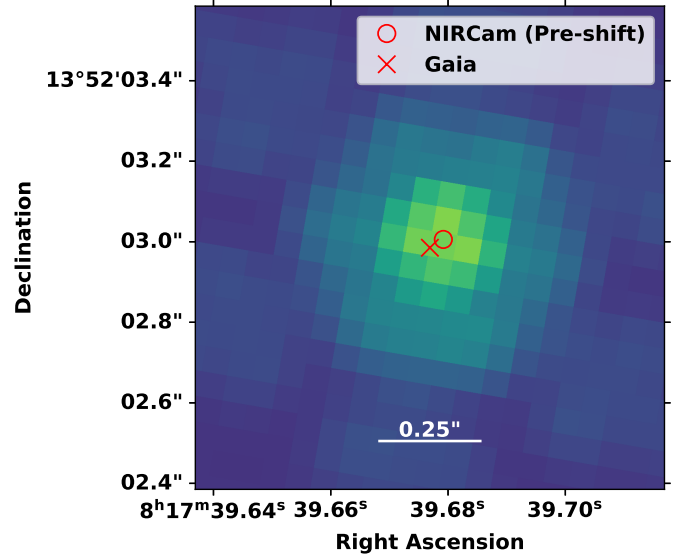


**Figure A1.** Astrometric verification of JWST/NIRCam F444W image (colour) retrieved from MAST archive. The best-fit centroid is shown by a red circle, while the Gaia DR3 position is shown by a red 'x'.

## APPENDIX A: ASTROMETRIC CORRECTION

Since we wish to compare the resolved morpho-kinematics of H $\alpha$  and [C II] emission, it is necessary to verify the astrometry of the JWST/NIRSpec IFU data. To do this, we align an archival JWST/NIRCam image to the Gaia DR3 reference frame (Gaia Collaboration et al. 2016, 2021), then align our NIRSpec data to this frame.

DLA0817g1 benefits from a wealth of existing archival data from space-based observatories, including HST WFC3/IR F160W (PID 15410, PI M. Neeleman), JWST/MIRI F770W and NIRCam F150W, F200W, F277W, F444W (PID 3954, PI F. Lelli), and JWST/NIRSpec IFU G395M/F290LP (PID 5761, PI M. Neeleman). Detailed SED fitting of this source will be performed in other works, and we only use the JWST/NIRCam F444W image to verify the astrometry of our NIRSpec IFU data. We download the calibrated (stage 3) JWST/NIRCam F444W image from MAST, as this is the only archival NIRCam image featuring spectral overlap with our NIRSpec data.

To begin, we search the Gaia DR3 catalogue<sup>10</sup> for stars near DLA0817g1. We choose the second closest star (Gaia DR3 650676554525737216), as the closest (Gaia DR3 650676344069432832) features large proper motion uncertainties. The position is corrected for proper motion since 2016, resulting in a shift of  $6.2 \pm 0.1$  mas (where the error includes uncertainties in the proper motion and initial position). The Gaia star is well-detected in the NIRCam image, so we determine its centroid by fitting a 2D Gaussian with LMFIT. The resulting position is offset from the Gaia position (see Figure A1) by  $39.2 \pm 2.3$  mas (where the error is taken from the uncertainty outputted by LMFIT). The NIRCam image is shifted to the Gaia astrometric frame by adjusting the values in the image header.

Next, we consider the NIRSpec IFU astrometry. Our R2700 data cube is convolved with the NIRCam F444W throughput curve ( $3.9 \leq$

<sup>10</sup> <https://gea.esac.esa.int/archive/>



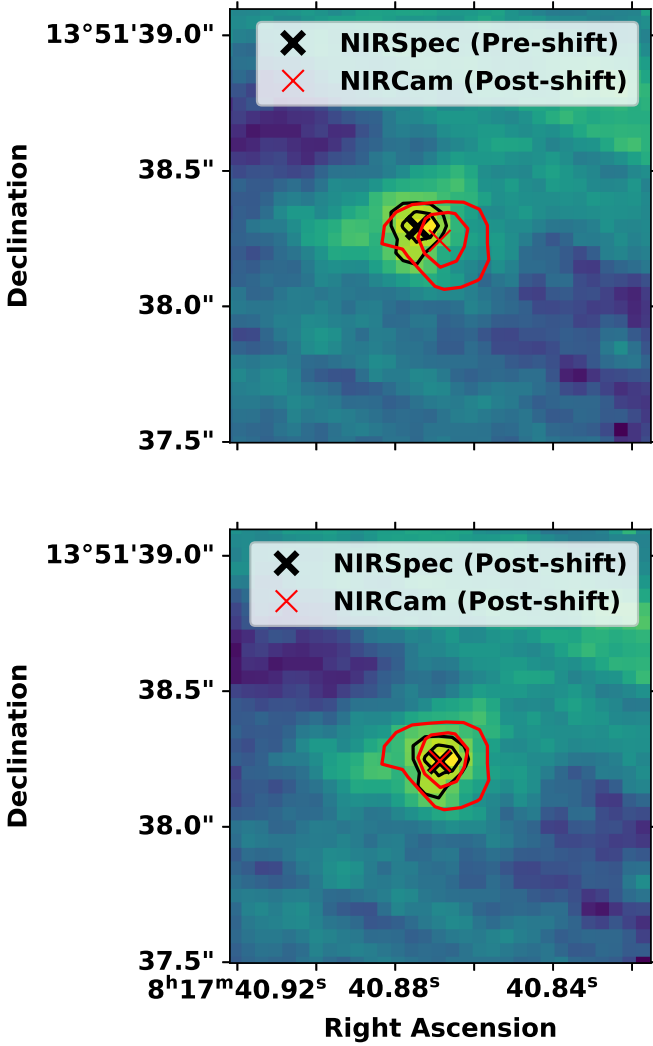


**Figure A2.** Application of astrometric correction to NIRSpec IFU data. Each panel shows the NIRCам F444W data (after alignment to the Gaia reference frame; red contours) compared to the convolved NIRSpec data (colourmap and black contours). In the top panel, we show the native NIRSpec data, while we align the NIRSpec data to the NIRCам data in the lower frame. Contours are shown at 80%, 90% of the maximum value in each map, and the best-fit centroid of each map is shown as a coloured cross.

( $\lambda_{\text{obs}}/\mu\text{m} < 5.1$ ), resulting in a pseudo-photometric map that we may compare with the NIRCам image. This comparison is not perfect, however, as the R2700 data feature a spectral gap near the centre of the F444W filter, resulting in a lower flux. While we will not use these data for flux calibration verification for this reason, they are still useful for spatial alignment.

The convolved NIRSpec image is shown in Figure A2 (colourmap and black contours), compared to the NIRCам data (red contours). Before spatial alignment, the two maps feature a spatial offset of  $95 \pm 9$  mas, which is comparable to the pointing uncertainty of NIRSpec with no target acquisition (Rigby et al. 2023). We align the NIRSpec data to the NIRCам reference frame by editing the image header. By combining all relevant uncertainties (i.e., Gaia star proper motion, Gaia star position, NIRCам image centroid, and NIRSpec image centroid) in quadrature, we find a total astrometric uncertainty of 6 mas.

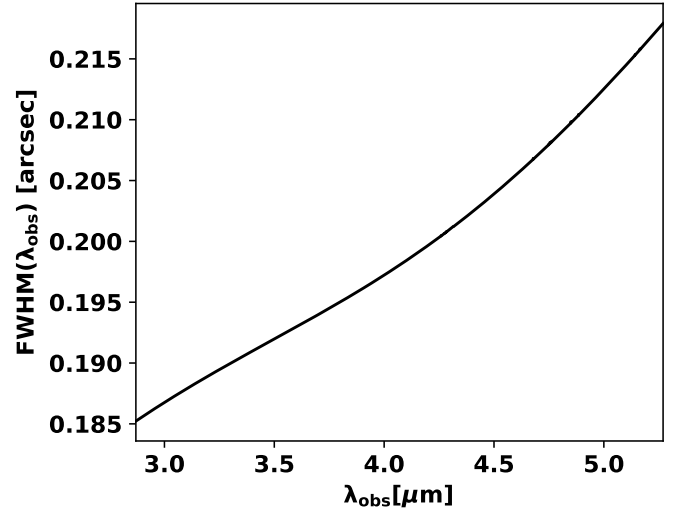


**Figure B1.** FWHM of the NIRSpec IFU PSF over the G395H/F270LP wavelength range, determined from a 2D Gaussian fit to the model PSF of STPSF.

From equation 10.7 of the ALMA technical handbook<sup>11</sup>, the positional uncertainty of ALMA is a function of the resolution and peak S/N. Using the values of the [C II] moment 0 map yields a positional uncertainty of  $\sim 14$  mas, or  $\sim 0.3$  spaxels in the NIRSpec IFU cube.

## APPENDIX B: PSF TREATMENT

While the JWST/NIRSpec IFU allows for high-resolution characterization of galaxies, it is vital to account for the wavelength-dependent behaviour of the PSF when comparing emission at different wavelengths. As noted by other works (e.g., Jones et al. 2025a), the NIRSpec PSF features both a central peak (which may be approximated by a Gaussian) and extended, low-level wings. In this Appendix, we use the code STPSF<sup>12</sup> to model the PSF of our data.

First, we use STPSF to create a model data cube of the PSF over the wavelength range of our data, fit a 2-D Gaussian model to the PSF at each wavelength, and record the geometric mean of the best fit FWHM of the major and minor axes (Figure B1). It is clear that the spatial resolution is degraded at redder wavelengths, with a variation of  $\sim 7.5\%$  from the mean ( $\sim 0.2''$ ).

To examine this in a different way, the top row of Figure B2 displays the finest PSF ( $\lambda_{\text{obs}} = 2.87 \mu\text{m}$ , panel a), coarsest PSF ( $\lambda_{\text{obs}} = 5.27 \mu\text{m}$ , panel b), and the difference the two (panel c). It is clear that assuming a constant PSF will result in residuals at all scales.

In order to ensure a fair comparison across all wavelengths of our data, we will force a common PSF ( $\text{PSF}_{5.27\mu\text{m}}$ ) across the data cube. For each wavelength of the cube, the necessary kernel is derived using the PHOTUTILS task `create_matching_kernel` (adopting a top hat window with  $\beta = 0.315$ ), and we use the astropy task `convolve` to perform the convolution. As an example, we show the derived kernel to transform  $\text{PSF}_{2.87\mu\text{m}}$  to  $\text{PSF}_{5.27\mu\text{m}}$  in panel d. The resulting

<sup>11</sup> <https://almascience.eso.org/documents-and-tools/cycle12/alma-technical-handbook>

<sup>12</sup> <https://stpsf.readthedocs.io/en/latest/>

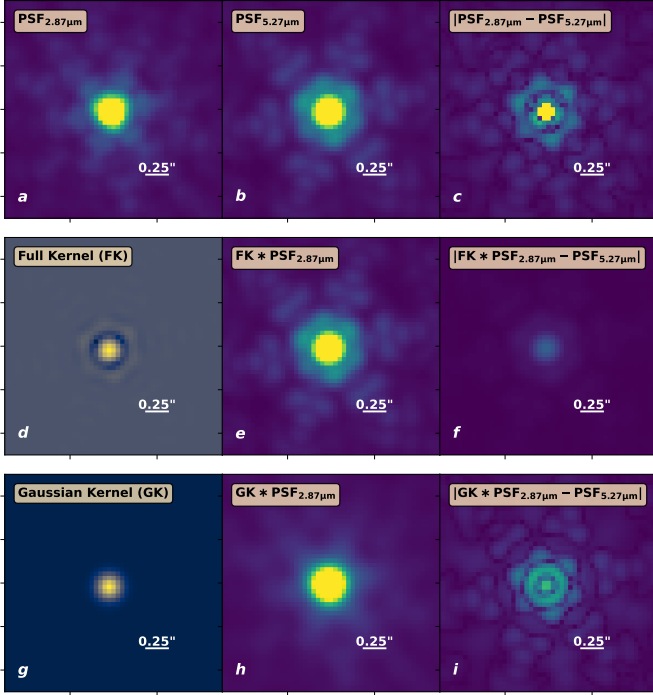


**Figure B2.** Demonstration of varying PSF size across our data cube, and our method of forcing a common PSF through custom convolution. The top row (a-c) shows the finest PSF, coarsest PSF, and the difference between them. The next two rows show kernels derived to match the two PSFs, using PHOTUTILS create\_matching\_kernel (‘Full kernel’, or FK; second row) and a Gaussian approximation of the resulting kernel (‘Gaussian kernel’, or GK; lower row). For each of these, we show the kernel, (d & g) the result of convolving the kernel with the finest PSF (e & f), and the residuals (f & i).

convolved PSF (panel e) is similar to PSF<sub>5.27μm</sub>, resulting in low residuals (panel f).

We emphasise that the convolution kernel is non-Gaussian, and that this method is preferable to a Gaussian convolution. Indeed, while the core of the convolution kernel is well described by a Gaussian kernel (panel g), if we convolve PSF<sub>2.87μm</sub> with a Gaussian kernel, the resulting convolved map lacks the wings of the real PSF (panel h), resulting in large residuals (panel i).

## APPENDIX C: POSTERIOR DISTRIBUTIONS OF ISM CONDITIONS

### APPENDIX D: FIR SED CONSTRAINTS

DLA0817g1 has been observed with ALMA in bands 3 and 4 (2023.1.00976.S; PI J. Prochaska), and in band 7 (2015.1.01564.S, 2017.1.01052.S; PI: M. Neeleman). This allows us to examine the dust properties of this source through FIR SED modelling. Here, we perform a preliminary inspection of the available data to gain a rough estimate of the dust mass in DLA0817g1, and defer a more in-depth analysis to future works.

First, we download the primary beam-corrected continuum images for each dataset from the ALMA archive, and measure the flux density of each in CARTA through 2D Gaussian fits. This results in strong detections in bands 4 and 7, and non-detections in band 3. Since the band 3 images feature large synthesized beams ( $FWHM \sim 2''$ ), we assume that DLA0817g1 is unresolved and estimate upper limits on

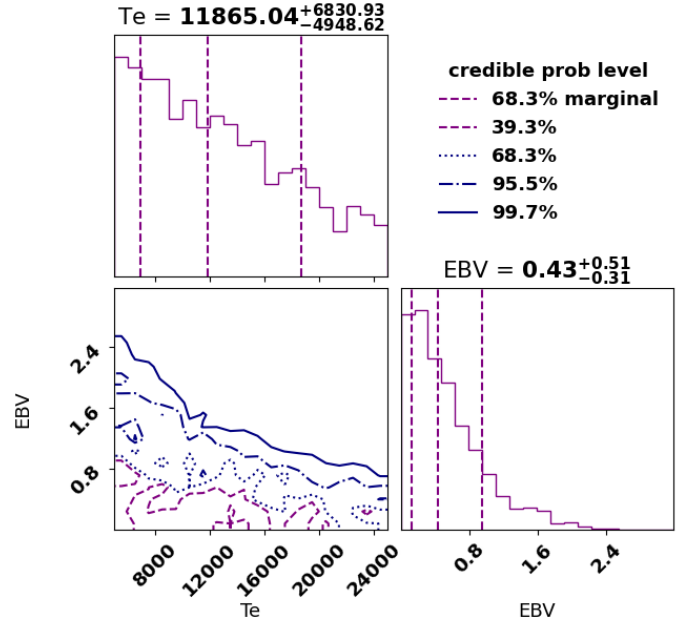


**Figure C1.** Posterior distributions and covariance plot for  $T_e$  and  $E(B - V)$ , as found through the procedure outlined in Section 3.3.

the flux density of  $3\times$  the RMS noise level. The resulting SED is shown in Figure D1.

To analyse this SED, we use a modified blackbody model (see Jones et al. 2020 for details) with variable dust temperature ( $T_{\text{dust}}$ ), dust emissivity index ( $\beta_{\text{IR}}$ ), and dust mass ( $M_{\text{dust}}$ ). Due to the low number of SED points, we do not proceed with a full modelling analysis at this time. Instead, we fix  $T_{\text{dust}} = 40$  K (based on the dust temperature evolution of Jones & Stanway 2023) and  $\beta_{\text{IR}} = 1.8$  (based on the findings of Wistok et al. 2023). Using ULTRANEST (Buchner 2021), we find that the data are best fit with a dust mass of  $\log_{10}(M_{\text{dust}}/M_{\odot}) = 7.98 \pm 0.04$  (Figure D1).

While constraints on these properties can be found through a more detailed analysis (i.e., combination of ALMA data in each band to produce optimal continuum images, improved flux density measurements, blackbody model fitting), we use our results to demonstrate that the FIR continuum emission of DLA0817g1 requires a substantial dust mass, which lies between SFGs ( $\sim 10^7 M_{\odot}$ ; e.g., Sommovigo et al. 2022) and SMGs ( $\sim 10^{7-9} M_{\odot}$ ; e.g., Wistok et al. 2023).

This paper has been typeset from a  $\text{\LaTeX}$  file prepared by the author.

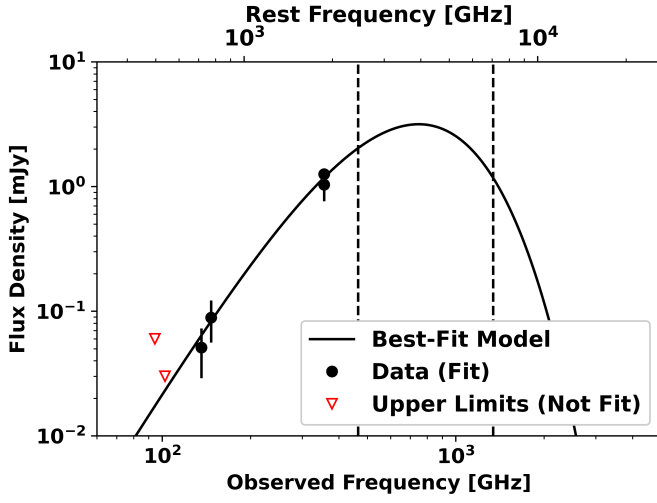


**Figure D1.** The FIR SED for DLA0817g1, including detections in bands 4 and 7 (black points) and non-detections in band 3 (red triangles). The best fit modified blackbody model (assuming  $T_{\text{dust}} = 40$  K,  $\beta_{\text{IR}} = 1.8$ ) is shown in black. The frequency range commonly used to measure  $L_{\text{FIR}}$  is denoted by the vertical black dashed lines.